Influence of post-processing treatments on fatigue limit of notched additive manufactured Ti-6AL-4V determined by rapid thermographic methodology

T. Dusautoir, Bruno Berthel, S. Fouvry, P. Matzen, K-D. Meck

Influence of post-processing treatments on fatigue limit of notched additive manufactured Ti-6AL-4V determined by rapid thermographic methodology.

T.Dusautoir[a,b,*] , B.Berthel[a,*], S.Fouvry[a], P.Matzen[b],K-D.Meck[b]

[a] Univ Lyon, Ecole Centrale de Lyon, CNRS, ENTPE, LTDS, UMR5513, 69130 Ecully, France

[b] John Crane, 31 Nash Road, Trafford Park, Manchester M17 1SS, United Kingdom

[*] Corresponding author.

E-mail address: theodusautoir@hotmail.fr, bruno.berthel@ec-lyon.fr

Abstract

This article explores how post-processing treatments affect the fatigue limit of additive manufactured Ti-6Al-4V in the presence of a stress gradient. Additive manufacturing (AM) technology enables manufacturers to create customized designs that can withstand specific loads, but it often results in complex shapes with stress gradients. Investigation into the influence of microstructure, internal porosity, and surface integrity on the fatigue limit of AM Ti-6Al-4V was conducted. Infrared imaging was used to detect and measure self-heating from which an estimate of the materials fatigue limit was derived. The study indicated that surface integrity is the most important factor to the fatigue life limit, and showed that the infrared thermography analysis provides a quick and accurate way to determine the fatigue limit, compared to the conventional staircase method.

Keywords: Additive manufacturing, stress gradient, thermography, fatigue, surface roughness

Nomenclature

A	surface area under roughness measurement
AC	air cooling
A_f	periodic signal amplitude at f_L
A_f^{sta}	A_f stabilized value
A_{2f}	periodic signal amplitude at $2f_L$
A_{2f}^{sta}	A_{2f} stabilized value
C_p	material specific heat
d	staircase stress step
E	Young modulus
%EL	percent elongation at failure
e	specimen thickness
F	tensile load
FC	furnace cooling
f_L	load frequency
f_s	camera frame rate
$J_{2,a}$	second invariant amplitude of the stress tensor deviator

K_t	stress concentration factor
$K_{t,net}$	net stress concentration factor
l	specimen section width
N_b	number of specimens used for the staircase method
N	number of cycles to failure
P_n	coefficients for the smoothing temperature function
r	notch radius
R	load ratio
s	standard deviation
S_a	surface averaged roughness
S_v	surface maximum pit height
T	specimen temperature
T^{ref}	unloaded specimen temperature
T_0	specimen initial temperature
T_0^{ref}	unloaded specimen initial temperature
Z	vertical coordinate of the surface topography for surface roughness measurement
ΔN	Number of cycles required for temperature stabilization
Δt	Rest time required for temperature stabilization
α	material constant used for the Crossland multiaxial fatigue criterion
α_k	material thermal expansion coefficient factor
σ_h	hydrostatic stress
σ_a	stress amplitude
$\sigma_{a,peak}$	peak stress amplitude
$\sigma_{a,peak,0}$	initial peak stress amplitude used for the staircase method
$\bar{\bar{S}}$	stress tensor deviator
σ_{d-1}	fatigue limit at R=-1
$\sigma_{d-1,str}$	peak stress amplitude fatigue limit at R = -1 determined by the staircase method
$\sigma_{d-1,IR}$	peak stress fatigue limit at R = -1 determined by the thermographic method
σ_c	Crossland equivalent stress
σ_{nom}	nominal stress
$\bar{\bar{\sigma}}$	stress tensor
σ_u	ultimate tensile strength
σ_{xx}	residual stresses in the $\vec{x}$ direction

σ_{y02}	yield strength at 0.2%
σ_{zz}	residual stresses in the $\vec{z}$ direction
ν	Poisson's ratio
ε	material emissivity
ρ	material density
θ_d	thermal drift
θ_d^{sta}	stabilized value of θ_d after several cycles
θ^{exp}	experimental temperature variation
θ^{fit}	fitted temperature variation
τ_{d-1}	torsion fatigue limit

1. Introduction

A flexible coupling is a device used to connect two machines at their shaft ends for the purpose of transmitting torque, accommodating misalignment and absorbing shock loads (*cf.* Fig. 1).

Fig. 1. Flexible mechanical coupling with an angular misalignment via lateral shaft offset.

To achieve a lighter and more optimized design, the coupling underwent topological optimization, resulting in a complex shape. Conventional manufacturing processes are not suitable for producing such a design whereas additive manufacturing (AM) offers a viable solution by enabling fast building directly from a computer aided design (CAD) object. Among various AM technologies, powder bed fusion (PBF) processes are particularly popular due to their ability to achieve high resolution and print quality [1–3]. However, PBF also has drawbacks as inherent to the process are material defects such as porosities, residual stresses, and high surface roughness [4]. Extensive research has been conducted on PBF Ti-6Al-4V alloy with numerous studies documenting and analyzing its characteristic defects [5–8]. These defects and microstructure heterogeneities are known to affect the fatigue performance of metals.

Surface integrity plays a significant role in the high-cycle fatigue (HCF) strength of materials. Machining can alter surface topography and surface layer properties, resulting in lower surface roughness and localized plastic deformation. One of the earliest studies on the influence of surface topography was conducted in 1923, as suggested by Novovic et al.[9], which demonstrating a decrease in fatigue limit for steel with increasing depth of machining scratches. This exhaustive review [9] suggests that surface roughness has a strong influence on HCF life for metals, particularly when the average roughness (R_a) exceeds 0.1μm. In the case of AM metals, the average surface roughness is typically higher compared to conventional metals. It varies depending on the material and process parameters such as layer thickness, heat input, and powder diameter [4]. For Ti-6Al-4V produced using PBF processes, studies have reported an average surface roughness ranging from 8 to 42μm depending on process parameters [10]. The high surface roughness is mostly due to the presence of non-melted powder particles sticking to the surface. Generally, laser beam powder bed fusion (L-PBF) tends to result in lower R_a compared to electron beam PBF (E-PBF). The poor surface quality adversely affects the fatigue limit of AM Ti-6Al-4V, as demonstrated in several studies [8,10–13]. The fatigue limit of as-built AM Ti-6Al-4V can be 50% lower compared to wrought

materials, as the surface irregularities act as micro-notches, promoting crack nucleation and premature failure [14–16].

Another aspect of surface integrity is the state of the surface layer. The layer build strategy, combined with a high heat input, creates a significant temperature gradient leading to the material expansion and contraction. This results in residual stresses that impact short crack growth and ultimately fatigue strength, although the effect is material dependent [9]. The aforementioned review suggests that for average surface roughness within a range of 2.5-5μm (R_a), residual stress is a better indicator of fatigue performance than surface topography. For Ti-6Al-4V, a comparison between similar surface topography achieved through machining with different surface layer states (with and without stress relief heat treatment) showed superior fatigue limits for the untreated material due to remaining compressive stresses [9]. In contrast, residual tensile stress has a negative impact on fatigue strength.

Considering these findings, it is crucial to reduce surface roughness or mitigate its influence to ensure sufficient fatigue endurance of components. Surface treatments can be employed for this purpose, and some specific treatments have been selected for this study to assess their impact on fatigue endurance.

Porosity is another inherent defect in AM metals. During the melting process, voids may form due to entrapped gas in the powder (gas atomized powder), resulting in spherical voids (gas pores). Insufficient penetration of the molten pool into the lower layer can generate elongated voids (lack of fusion defects) [4]. These voids can serve as nucleation sites for cracks, leading to lower fatigue strength and higher dispersion compared to conventional materials [12,17,18]. Similar defects and microstructure heterogeneities have been observed in cast aluminum alloys, and their influence on fatigue strength has been investigated[19–21]. The harmfulness of these defects is typically characterized by their type, size, morphology, and position. Fatigue failure generally occurs at the most critical defect, which is why failure prediction models often use a probabilistic approach based on the weakest link concept [19,22–24]. In this study, the influence of porosity defects on fatigue strength is compared with different levels of surface roughness.

Another important aspect to consider is the material microstructure. The PBF processes generates specific microstructures, with columnar and equiaxed grain morphologies being the most common [4]. In L-PBF Ti-6Al-4V, the high cooling rates result in the formation of α' martensite phase in the form of fine laths, while in E-PBF, the α phase is present as lamellae [25]. Dendrites exhibit vertical growth (parallel to the build direction), leading to the formation of β columnar grains, as highlighted in [26]. The preferred orientation of the microstructure can lead to potential mechanical properties anisotropy, making equiaxed microstructures desirable, although they are more challenging to achieve. Notably, there is a significant difference in ductility between L-PBF and E-PBF Ti-6Al-4V. L-PBF parts tend to be more brittle due to the presence of the martensite phase, but they have higher yield strength. If fatigue failure is influenced by the microstructure, crack nucleation and propagation are primarily driven by the morphology of the α phase, with the presence of fine α needles, plates, or colonies generally being beneficial [27].

In industrial operations, couplings undergo complex multi-axial fatigue loading, with stress gradients induced by their geometry. The presence of stress gradients has a significant impact on the fatigue behavior, regardless of whether the stresses are unidirectional or multidirectional. Distinguishing between stress gradient and size effect can be challenging since both factors can occur simultaneously. The work of Papadopoulos and Panoskaltsis highlights the dependence of fatigue limits on stress gradients through a rotating bending test analysis, where the specimen length is kept constant while the radius is increased. The results demonstrate that higher stress gradients correspond to higher fatigue limits [28].

Therefore, it was considered important to investigate the fatigue behavior of AM Ti-6Al-4V in the presence of a stress gradient that reflects real industrial conditions. This characterization aims to understand the influence of defects under a gradient. The study focuses on examining the impact of post-processing treatments, including surface treatments and heat treatments, on the fatigue limit of L-PBF Ti-6Al-4V alloy. While it would be ideal to test the actual component under industrial conditions, the production of multiple AM couplings is cost prohibitive. Bridging the gap between life prediction based on laboratory test specimens and real-life components is challenging, especially for AM parts, considering the potential differences that can exist between seemingly similar parts. Notably, microstructures and defect features can vary across different positions and orientations on the build platform [29,30]. Hence, an equivalent specimen was designed to undergo similar loading conditions as the coupling. A stress gradient is induced by incorporating notches, and the strategy for achieving this tailored design will be described later in this paper.

Traditional methods for determining fatigue properties are time-consuming and require expensive destructive techniques that yield scattered results. To address these limitations, alternative approaches have been developed that utilize the self-heating response of a material to assess fatigue limits under both uniaxial [31–33] and multiaxial [34,35] loading conditions. These methods rely on the assumption that temperature changes in the specimen during a fatigue test can indicate microscopic plasticity. While these techniques have been applied to AM materials [36–39] there is limited research on AM titanium alloys specifically. However, studies can be found on conventionally manufactured titanium alloys [40–42]. Therefore, this work is original as it employs self-heating measurements on AM Ti-6Al-4V alloy under the presence of a stress gradient induced by notches.

For this study, an infrared thermographic technique is used to compare the fatigue strength of the L-PBF Ti-6Al-4V alloy that has undergone different post-processing treatments. After the introduction, the article proceeds with a detailed description of the development of the equivalent test specimen design. This section outlines the specific design considerations and factors considered to create a specimen that mimics the loading conditions experienced by the coupling. Next, the materials used in the study and the post-processing treatments applied to the specimens are described. Following the description of the materials and post-processing treatments, the article presents the infrared thermographic technique employed in the study. Subsequently, the results obtained from the experiments are presented. The focus is on the effects of surface finish and microstructure on the HCF strength of the AM Ti-6Al-4V alloy under the presence of a stress gradient.

2. Material and experimental method

2.1. Laboratory test specimen design

As mentioned earlier, the aim of this study is to investigate the HCF strength of Ti-6Al-4V couplings manufactured using L-PBF technology. To make the study feasible, a laboratory specimen was designed to be lighter and more cost-effective than the original part. However, it was crucial to ensure that the stress state in the specimen accurately represented the conditions experienced by the coupling in industrial settings. Three key considerations were identified:

- Description of cyclic loading: couplings undergo cyclic multi-axial stresses due to shaft misalignments and complex geometries. To account for this, a multi-axial fatigue criterion was used to convert the cyclic load into an equivalent scalar stress value [43].
- Incorporation of high stress gradients: geometries resulting from topological optimization can be highly complex and prone to high stress gradients, which are known to impact fatigue performance [28].
- Consideration of size effect: larger parts may exhibit lower fatigue performance due to a higher probability of encountering material defects [44].

The Crossland multi-axial fatigue criterion was chosen to characterize the cyclic loading. This criterion calculates the maximum shear stress amplitude by taking the square root of the second invariant of the stress tensor deviator amplitude $\sqrt{J_{2,a}}$ and the maximum hydrostatic stress $\sigma_{h,max}$ [45].

$$\sigma_c = \sqrt{J_{2,a}} + \alpha\sigma_{h,max} \leq \tau_{d-1} \tag{1}$$

where $\alpha = 3\,\tau_{d-1}/\sigma_{d-1} - \sqrt{3}$, $\sigma_{h,max} = \max_t \frac{1}{3}\mathrm{tr}(\bar{\bar{\sigma}}(t))$

$$\sqrt{J_{2,a}} = \frac{1}{2}\sqrt{\frac{1}{2}\max_{t_0 \in t}\left[\max_{t_0 \in t}\left[(\bar{\bar{S}}(t) - \bar{\bar{S}}(t_0)) : (\bar{\bar{S}}(t) - \bar{\bar{S}}(t_0))\right]\right]} \tag{2}$$

Finite element method (FEM) analysis using ABAQUS 6.14 was performed on three different versions of AM couplings. The load is defined as a combination of a constant torque and alternating angular misalignment. The elements used are C3D20R, which are 20-node quadratic bricks with reduced integration.

In critical areas, a minimum element length of 0.1mm is employed, as shown in Fig. 2. To compute the Crossland equivalent stress and hydrostatic stress gradient, a Python sub-routine is utilized. The norm of the hydrostatic stress gradient is determined based on the invariant formulation described by Papadopoulos and Panoskaltsis [28]:

$$\left\|\overrightarrow{\nabla\sigma_h}\right\| = \sqrt{\left(\frac{\partial\sigma_h}{\partial x}\right)^2 + \left(\frac{\partial\sigma_h}{\partial y}\right)^2 + \left(\frac{\partial\sigma_h}{\partial z}\right)^2} \quad (3)$$

For size effect consideration, specimen thickness is equivalent to the thickness at the hotspot. This ensures that the specimen reflects the same thickness as the original coupling, considering the potential influence of size on fatigue performance.

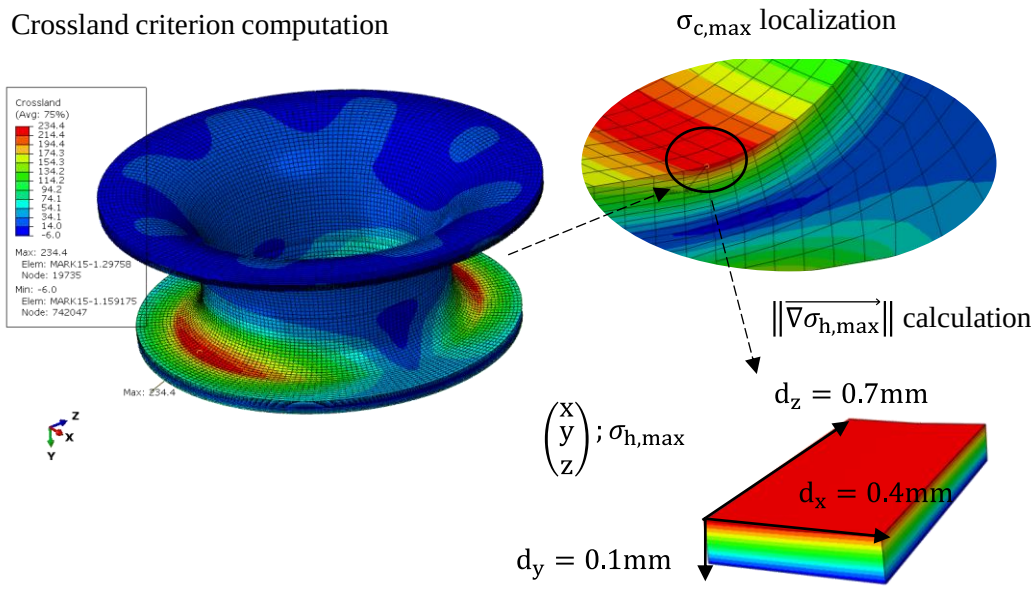

Fig. 2. Illustration of the resultant Crossland equivalent stress field on the AM coupling under industrial load conditions, computed through FEM analysis. Post-treatment involves localizing the peak Crossland equivalent stress and computing the hydrostatic stress gradient.

To replicate the stress gradient, a double semi-circular notched thin plate design (C-notched) is chosen, as shown in Fig. 3. The resulted local peak stress is calculated by multiplying the nominal stress by a concentration factor known as K_t, which depends on the geometry of the notch. The stress gradient intensity is influenced by the radius of the notch, with lower radii resulting in higher stress gradients.

FEM simulations are performed using the same methodology to converge on the desired values. The FEM results are presented in Fig. 4. It is observed that the closest match to the average results of the coupling ($\left\|\overrightarrow{\nabla\sigma}\right\|$, $\sigma_{eq,max}$) is achieved with a notch radius of 1mm. This notch radius corresponds to a stress concentration factor, $K_{t,net}$, of 2.54 according to Peterson's equation [46] :

$$K_{t,net} = \frac{\sigma_{peak}}{\sigma_{nom,net}} = 3.065 - 3.472\left(\frac{2r}{w}\right) + 1.009\left(\frac{2r}{w}\right)^2 + 0.405\left(\frac{2r}{w}\right)^3 \quad (4)$$

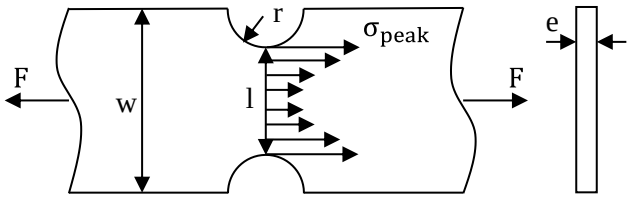

Fig. 3. Laboratory double C-notched specimen with l=10mm, e=2mm, r=1mm.

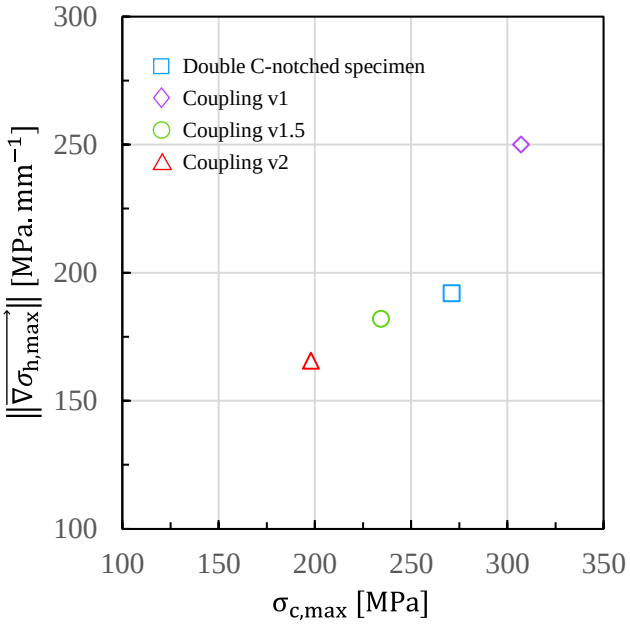

Fig. 4. Norm of the maximum hydrostatic stress gradient according to the maximum Crossland equivalent stress resulted from FEM analysis for multiple coupling versions and the laboratory double C-notched specimen.

2.2. Material

2.2.1. Powder, process parameters and mechanical properties

The couplings and test specimens in this study were fabricated using Ti-6Al-4V gas atomized powder and processed through the direct metal laser sintering (DMLS) technique using the EOS M290 machine. The manufacturing process was overseen by an external supplier, with the layer thickness set at 60µm as the disclosed processing parameter. Table 1 provides the chemical composition of both the powder and the built solid part.

To mimic industrial conditions, the manufacturer was allowed to choose the process parameters, resulting in the corresponding material properties. However, the build direction was selected as a controllable parameter due to its significant influence on surface roughness and microstructure. Previous studies by Nicoletto et al. [47] revealed that the build strategy affects surface roughness and subsequent fatigue response. Vertically built specimens exhibited the poorest surface roughness and lowest fatigue limit compared to horizontally built ones. Furthermore, vertically built Ti-6Al-4V specimens in another study demonstrated improved ductility but lower yield stress, indicating mechanical anisotropy attributed to microstructure orientation [48].

Considering the objective of replicating the couplings' characteristics, a vertically build strategy was chosen for the laboratory test specimen, as shown in Fig. 5. Coupling's build angle was 45°, this angle aligns the critical area defined by FEM and Crossland computation parallel to the build direction. Besides, opting for the most challenging process strategy is justified due to the complex geometries resulting from topology optimization in the design of AM couplings, which can have varying build orientations.

Table 2 presents dimensional characteristics of the powder and mechanical properties of the AM Ti-6Al-4V material. Tensile tests were performed using an INSTRON 100KN electromechanical testing machine, and the deformation fields were captured using a digital image stereo-correlation (DIC) system (two 4M pixels CCD cameras AVT Pike F-421B and Vic 3D v7 software) following the method described in [49]. The ultimate tensile strength and yield strength were found to be relatively high compared to conventional Ti-6Al-4V, but the ductility was relatively low. It is worth noting that a stress relief heat treatment was applied, and the surface state remained as-built.

Table 1. The provided data represents the weight percentages of the elements in the Ti-6Al-4V powder, and Ti-6Al-4V solid part as provided by the manufacturer.

Element [wt.%]	Ti	Al	V	Fe	O	C	N	H
Powder	Bal.	6.26	3.94	0.20	0.13	<0.01	0.01	0.002
Solid part	Bal.	6.10	3.96	0.20	0.17	<0.01	0.03	0.004

Table 2. Ti-6Al-4V powder size distribution, density of the powder and the solid part, all provided by the supplier. While the mechanical properties were obtained through 3 tensile tests using digital image stereo-correlation (DIC) analysis.

	Size characteristics [µm]			Density [g/cm^3]	Young Modulus E [GPa]	Poisson's ratio ν	Ultimate tensile strength σ_u [MPa]	Yield strength at 0.2% σ_{y02} [MPa]	Percent elongation %EL [%]
	d10	d50	d90						
Powder	25	40	56	4.405	-	-	-	-	-
Solid part	-			4.4	118.7	0.31	1077	1021	8

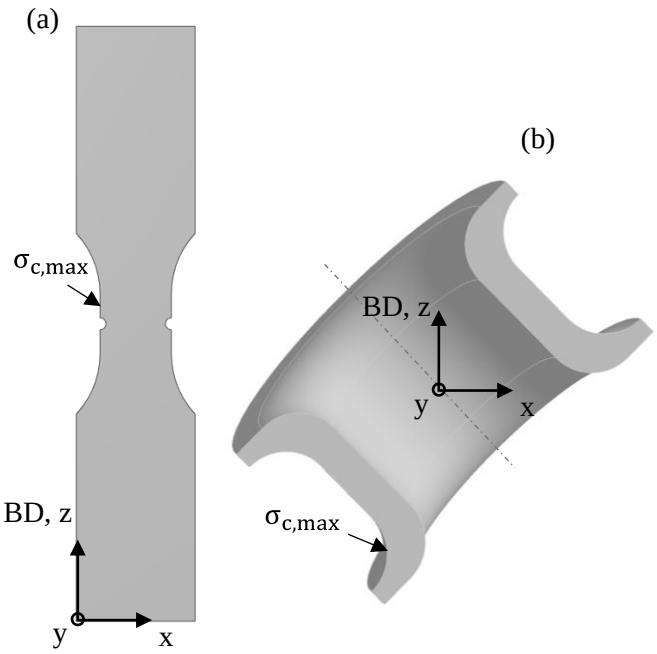

Fig. 5. Laboratory C-notched specimen (a) and coupling middle section (b) orientations according to the build direction (BD) during L-PBF manufacturing process.

2.2.2. Surface integrity

One commonly used surface treatment for enhancing the fatigue strength of components is shot peening. This technique involves impacting a surface with round metallic, glass, or ceramic particles with a force sufficient to create plastic deformation and generating compressive stresses near the surface [9,50]. Within certain intensity limits, shot peening can contribute to the improvement of fatigue strength, primarily by reducing the mean stress level [51]. After the L-PBF process, the specimens typically undergo a stress relief heat treatment to prevent distortion during removal from the base plate. This treatment helps to partially remove residual stresses. Since measuring the Almen intensity is not feasible, which is a shot peening intensity scale [52], the term "shot peening" is replaced with "blasting" in this study. Blasting is a simple surface treatment that can be easily applied on AM couplings, here it involves applying alumina abrasive

particles with an approximate size of 250µm, followed by ceramic micro-beads particles ranging in size from 63 to 125µm. A constant pressure of 7 bars is applied, and both sides of the specimen, as well as the roots of the notches, are treated.

Another surface treatment investigated in this study is chemical etching. It involves immersing the specimen in an acid bath composed of hydrofluoric and nitric acids. The acids attack the material, causing oxidation, and a complexing agent is used to solubilize the oxide layer. This process leads to the gradual dissolution of surface peaks and valleys resulting in a better surface state. The decline in surface roughness depends on the exposure time and the amount of material removed. Additionally, a combination of chemical etching and ceramic micro-beads blasting is also tested.

These surface treatments are compared to a conventional machining process, specifically milling. However, machining is not a suitable solution for AM metal parts due to the complexity of their geometries, which often restricts access to machining tools.

Surface topography is characterized using a 3D Wyko NT9300 optical profilometer from VEECO, which provides surface roughness measurements with a vertical resolution of 3nm. The measurements are preformed within the notch root area, where the surface roughness is the highest and stress concentration is also significant. Two basic parameters, S_a (averaged surface roughness) and S_v (maximum pit height) equation (5), are used to quantify the surface roughness and enable meaningful comparisons between different surface topographies. The results of the surface roughness measurements are presented in Table 3 and 3D visualizations of the surface topographies are shown in Fig. 6.

$$\begin{cases} S_a = \dfrac{1}{A}\iint_A |Z(x,y)|\,dx\,dy \\ S_v = \left|\min_A Z(x,y)\right| \end{cases} \tag{5}$$

The as-built material unsurprisingly exhibits the poorest roughness. On the 3D roughness profile, significant asperities resulting from non-melted powder particles are visible, *cf*. Fig. 6 (a). Logically, the roughness within the notch tip is higher compared to the rest of the specimen. This is attributed to the slight challenge posed by inserting a 1mm notch radius in the AM process, which generates numerous peaks and valleys, thereby creating multiple potential nucleation sites. The application of blasting reduces the average surface roughness by approximately 50%, with a slightly lower reduction in pit depth. Examination of the surface's 3D profile reveals the elimination of unmolten powder particles through the blasting process, resulting in smoother and rounder peaks, *cf*. Fig. 6 (b). On the other hand, chemical etching leads to a reduction in S_a from 28 to 8µm, corresponding to a 70% decrease. Despite the presence of pits caused by chemical reactions, a smoother surface is achieved, *cf*. Fig. 6 (c). Additionally, the introduction of blasting further reduces roughness by flattening these pits, *cf*. Fig. 6 (d).

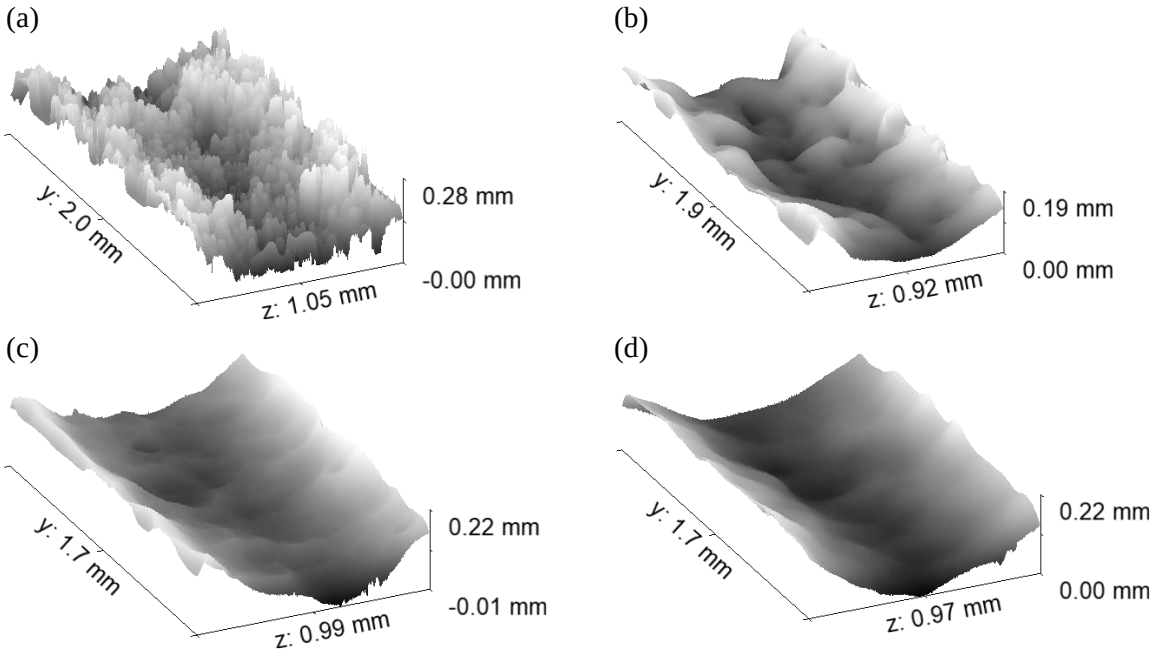

Fig. 6. 3D visualizations of surface topographies of L-PBF Ti-6Al-4V in (a) as-built (b) blasted (c) chemical etched and (d) chemical etched + blasted surface states.

Table 3. Surface roughness measurements of L-PBF Ti-6Al-4V according to different surface treatments.

Surface state	S_a (µm)	S_v (µm)
AM Ti64 AB (as-built)	28.4 ± 1.9	117.6 ± 42.5
AM Ti64 Blasted	13.5 ± 1.7	69.5 ± 13.9
AM Ti64 Chemical Etched (CE)	8.1± 1.0	37.9 ± 7.4
AM Ti64 CE & Blasted	7.7± 1.4	31.2 ± 6.5

2.2.3. Microstructure and internal defects

As previously mentioned, all the specimens underwent a stress relief heat treatment. Additionally, both sub-transus and super-transus heat treatments were performed on the blasted and machined specimens. Vrancken et al. [53] evaluated the effects of these heat treatments on the mechanical properties of PBF Ti-6Al-4V but not on fatigue properties. The tested materials are listed in Table 4 and the resulting microstructures are presented in Fig. 7. The samples were polished using silicon carbide (SIC) (P600 to P2400) and diamond suspension of 3µm and 1µm. A final step was performed using colloidal silica suspension. A chemical attack with KROLL reagent was necessary to reveal the microstructure.

After the stress relief heat treatment, a textured microstructure with prior β columnar grains along the build direction (YZ plan on Fig. 7) is observed after stress relief heat treatment. At a smaller scale, there is a mixture of α (white) and β (black) phases, with α appearing as fine needles.

Following the sub-transus heat treatment, elongated grains along the build direction remained, but with larger α grain boundaries. Furthermore, the α needles were replaced by α lamellae surrounded by β, arranged in a basket weave structure.

For the super-transus heat treatment, above the β transus temperature, the columnar grains transformed into large semi-equiaxed grains, resulting in a homogeneous microstructure. At a smaller scale, the microstructure is similar but with coarser grain boundaries. At such temperatures, the cooling rate plays a role in controlling the size of the α plates [53].

The stress relief treatment is crucial as it suppresses the martensitic structure, which has the disadvantage of significantly reducing ductility [53]. It also relieves residual stresses resulting from the AM process. However, the lamellar microstructure formed by the sub-transus heat treatment is somewhat coarser, which increases ductility but contributes to a decrease in yield strength. The influence of these heat treatments on L-PBF Ti-6Al-4V in terms of fatigue behavior is not well-known. However, in [54] the authors gathered

data from earlier research works and found that lamellar microstructures have better HCF strength than bimodal microstructures but lower than equiaxed microstructures. For lamellar microstructures, the fatigue strength is determined by the width of the α lamellae, with fatigue strength decreasing as the α lamellae width increases. In our case, the α lamellae are larger with the sub-transus and super-transus heat treatments compared to the stress relief heat treatment. The morphology of the prior β grains undergoes significant changes between the sub-transus and super-transus conditions, suggesting that different fatigue behavior can be expected.

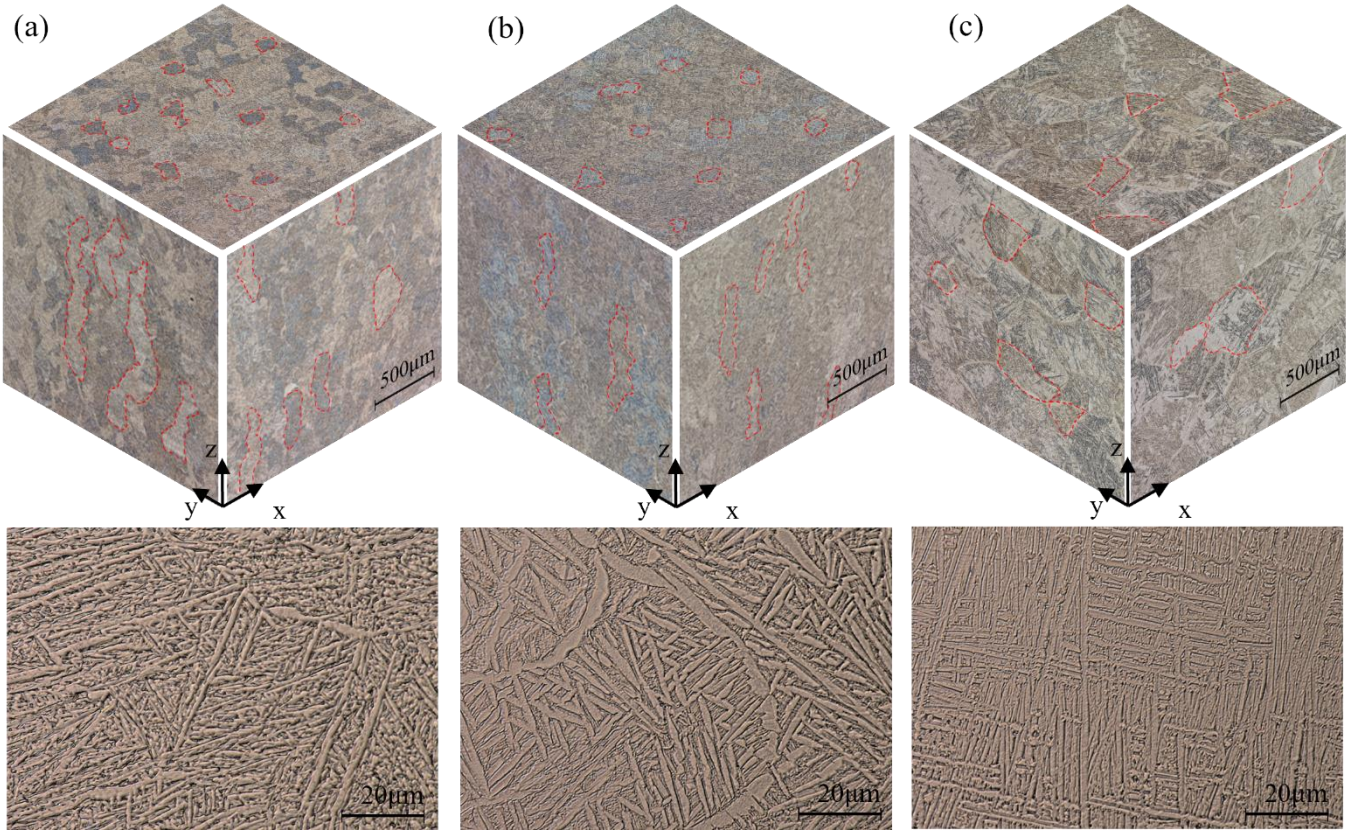

Fig. 7. Microstructures of L-PBF Ti-6A-4V after (a) stress relief (b) sub-transus (c) super-transus heat treatment.

Table 4. Overview of examined materials: surface treatments and heat treatments.

Material configuration	Surface treatment	Heat treatment
AM Ti64 AB (as-built)	X	Stress relief 800°C 2h + FC
AM Ti64 Blasted	Blasting with alumina abrasive and ceramic microbeads	Stress relief 800°C 2h + FC
		Sub-transus: 940°C 1h +AC 650°C 2h + AC
		Super-transus: 1015°C 0.5h +AC 730°C 2h + AC
AM Ti64 Chemical Etched (CE)	Chemical etching	Stress relief 800°C 2h + FC
AM Ti64 CE & Blasted	Chemical etching followed by blasting with ceramic microbeads	Stress relief 800°C 2h + FC
AM Ti64 Machined	Milled	Stress relief 800°C 2h + FC
		Sub-transus: 940°C 1h +AC 650°C 2h + AC
		Super-transus: 1015°C 0.5h +AC 730°C 2h + AC
Ref Ti64	Milled	X

2.3. Experimental method

2.3.1. Staircase fatigue tests

The staircase method, a statistical approach, is utilized to estimate the fatigue limit and its standard deviation [55]. Table 6 provides a summary of the procedure parameters, fatigue limits, and their corresponding standard deviations when Dixon and Mood conditions are met. In this study, fully reversed uniaxial fatigue tests (R=-1) are performed on an MTS servo-hydraulic testing machine. The tests are conducted at a frequency of 40 Hz, with the load following a sinusoidal signal. The maximum number of cycles for the fatigue tests is set at 10^7 cycles.

2.3.2. Infrared thermographic technique

The device used to measure the temperature evolution is a FLIR SC7600 MWIR 2.5-5μm infrared camera equipped with an optical lens of 25 mm focal length. The noise-equivalent temperature is lower than 25 mK with a maximum frequency of 380 Hz. In this study, each pixel corresponds to a zone with dimensions of 0.08×0.08mm². Prior to each experiment, the Infrared (IR) camera was calibrated using a pixel-to-pixel calibration method, similar to the approach described in [56]. The calibration involved the use of a laboratory blackbody (SR 800R by CI-system), which offers a surface temperature accuracy of ±0.006°C for temperatures ranging from 0 to 50 °C and a thermal uniformity of ±0.015 °C.

To enhance emissivity and prevent camera reflection on the tested material, the specimens are coated with a matte black paint. To measure emissivity, an indirect measurement technique based on spectral reflectivity is employed, as described in [57]. The experimental method is similar to the approaches outlined in [58,59]. In this method, a black body emits infrared radiation towards the surface of the specimen, and the IR camera captures the reflected radiation. The incidence angle is set to 30°. The emissivity (ε) of the various surface states of the materials is evaluated for three different black body temperatures: 25°C, 35°C, and 50°C. The measured emissivity values are presented in Table 5. Remarkably, despite the heterogeneity of surface roughness, the emissivity values are very close and nearly equal to 1 for all the surface states.

Table 5. Emissivity measurements of L-PBF Ti-6Al-4V obtained with indirect reflectivity method for three temperatures (25,35 and 50°C).

Surface state	ε_{mean}	Standard deviation
AM Ti64 AB (as-built)	0.96	5E-04
AM Ti64 Blasted	0.98	17E-04
AM Ti64 Chemical Etched (CE)	0.98	19E-04
AM Ti64 CE & Blasted	0.94	36E-04
AM Ti64 Machined	0.96	28E-04

During the fatigue test, the camera is positioned in front of the specimen and remains stationary throughout the test. It continuously monitors the temperature evolution of the loaded specimen, as well as an unloaded reference specimen placed on the frame. To minimize any potential environmental effects on the thermal fields and maintain stable thermal boundary conditions, both the camera and the specimens are enclosed within an insulation box. This insulation box helps to regulate the temperature and reduce the influence of external factors. The experiments are conducted at room temperature to ensure consistent and controlled testing conditions.

The experimental set-up is illustrated in Fig. 8. The specimen is subjected to alternating tensile and compressive loads with a stress ratio (R=-1) at a frequency of 30Hz. The load is incrementally increased until the specimen fails. The IR camera tracks the specimen temperature evolution at a frequency of 19Hz. To capture environmental temperature variations, the surrounding environment temperature is approximated by the temperature of the reference specimen. By subtracting the reference specimen temperature from the specimen temperature evolution, the material temperature drift θ is obtained. The initial temperature T_0 before each load increment is also recorded. This process applies to each pixel of the temperature map captured by the IR camera.

Analyzing the temperature evolution shown in Fig. 8, it can be observed that the material initially heats up until the temperature stabilizes. Once the stabilization is reached, the temperature starts to decrease, returning close to its initial level. Typically, a sufficient number of $\Delta N = 10\,000$ cycles is required for temperature stabilization, and a rest time Δt of 5 minutes load increments is necessary to allow the material to cool down.

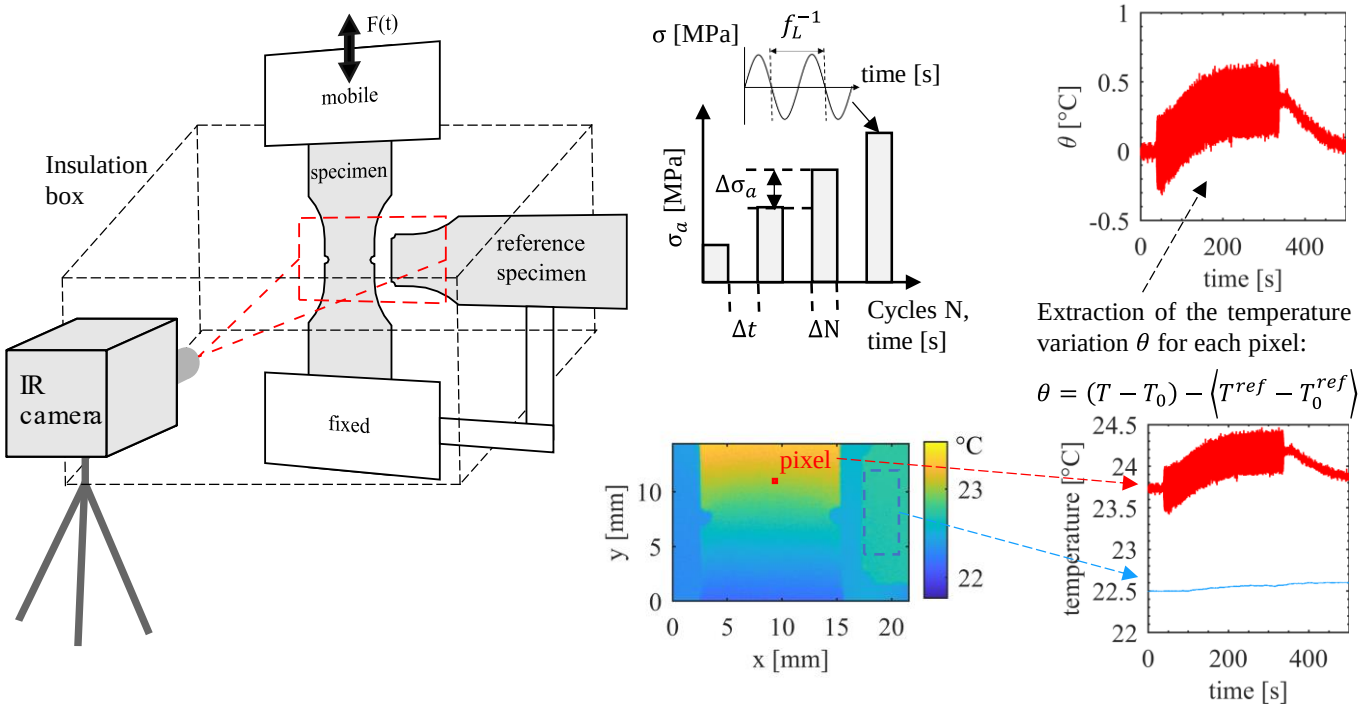

Fig. 8. Set-up of the thermographic method. Specimen temperature evolution monitoring during fatigue test via an infrared camera.

For the post-treatment, the methodology used is similar to the one presented by Berthel et al. [60]. To individually analyze each effect on the thermal signal, a sliding-smoothing technique using least-squares is applied to each pixel of the captured data. One of the main advantages of this method is its ability to work with an under-sampled signal, the Nyquist–Shannon sampling principle is not respected. With the correct ratio between the sampling rate and the frequency of the signal, it allows the extraction of various heating variables from a single thermal signal [58]. The smoothing temperature function, θ^{fit}, is expressed as follows [60]:

$$\theta^{fit} = \underbrace{p_1 + p_2 t}_{\text{thermal drift}} + \underbrace{p_3 \cos(2\pi f_L t) + p_4 \sin(2\pi f_L t)}_{\text{periodic function at } f_L} + \underbrace{p_5 \cos(4\pi f_L t) + p_6 \sin(4\pi f_L t)}_{\text{periodic function at } 2f_L} \quad (6)$$

Where the periodic signal at f_L describes the thermoelastic effects, which are related to the cyclic loading and resulting thermal responses of the material. This signal captures the variations in temperature due to the mechanical stresses applied during the fatigue test. On the other hand, the linear drift θ_d and the periodic signal at $2f_L$ represent transient effects due to heat loss, dissipative heating and possible drifts in the equilibrium temperature. The p_n parameters are fitted constant parameters and are estimated for each pixels.

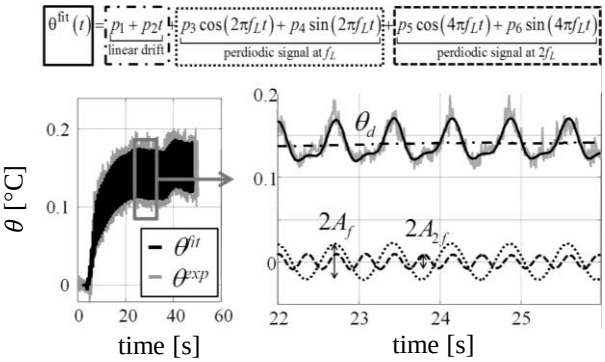

Fig. 9. Example of the moving least-square fitting method [60].

Thermal drift, θ_d, and amplitudes of periodic signals at f_L and $2f_L$, respectively A_f and A_{2f} (*cf.* Fig. 9) are defined by :

$$\begin{cases} \theta_d = p_1 \\ A_f = \sqrt{p_3^2 + p_4^2} \\ A_{2f} = \sqrt{p_5^2 + p_6^2} \end{cases} \quad (7)$$

The thermal drift and the signal amplitudes reach stabilized values (θ_d^{sta}, A_f^{sta}, A_{2f}^{sta}) after a few cycles (*cf.* Fig. 10). The evolutions of θ_d^{sta} and A_{2f}^{sta} are particularly important as they can provide insights into the dissipative heating effects and their relationship to microplasticity. Note that it is the maximum values of A_f^{sta}, θ_d^{sta} and A_{2f}^{sta} values are that extracted within a zone of interest (ZOI) close to the notch root where the stress is the highest (*cf.* Fig. 11). Consequently, results are not dependent of the dimension and location of the ZOI but rather dependent of the pixel size which is 0.08×0.08mm²

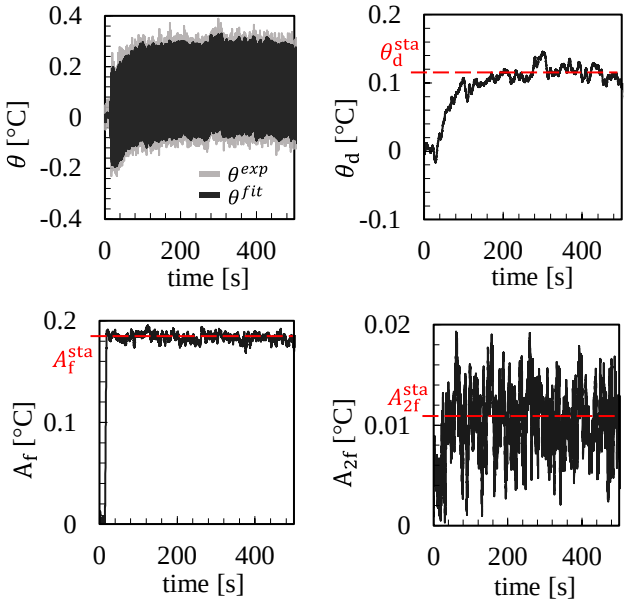

Fig. 10. Evolutions of θ^{exp}, θ^{fit}, θ_d, A_f and A_{2f} of as-built L-PBF Ti-6Al-4V during uniaxial fatigue test (R = -1) at a load frequency of 30Hz.

An example of results obtained from a fatigue test performed on L-PBF Ti-6Al-4V in as-built surface state condition is provided in Fig. 11. The maximums values of θ_d^{sta}, A_f^{sta} and A_{2f}^{sta} in the ZOI are determined for each stress step, and they are plotted as a function of the peak maximum stress near the notch tip. Three distinct evolutions can be observed from the plots of θ_d^{sta} and A_{2f}^{sta}.

I: At low stress levels, the temperature evolution remains stable, indicating a relatively mild thermal response of the material. II: As the stress level exceeds a certain threshold, the temperature increases exponentially, suggesting the presence of micro-plasticity mechanisms within the material. III: Subsequently, cracks start to form and propagate, leading to significant heating of the material. This is evident from the notable increase in temperature recorded. In accordance with the theory of thermoelasticity the evolution of A_f^{sta} is linear until the onset of plasticity phenomena [61]. The recorded images displayed in Fig. 11 reveal that the heating primarily occurs at the notches tips and subsequently follows the path of the cracks as they propagate through the material. This observation provides valuable insight into the thermal behavior and failure mechanisms of the material during the fatigue test.

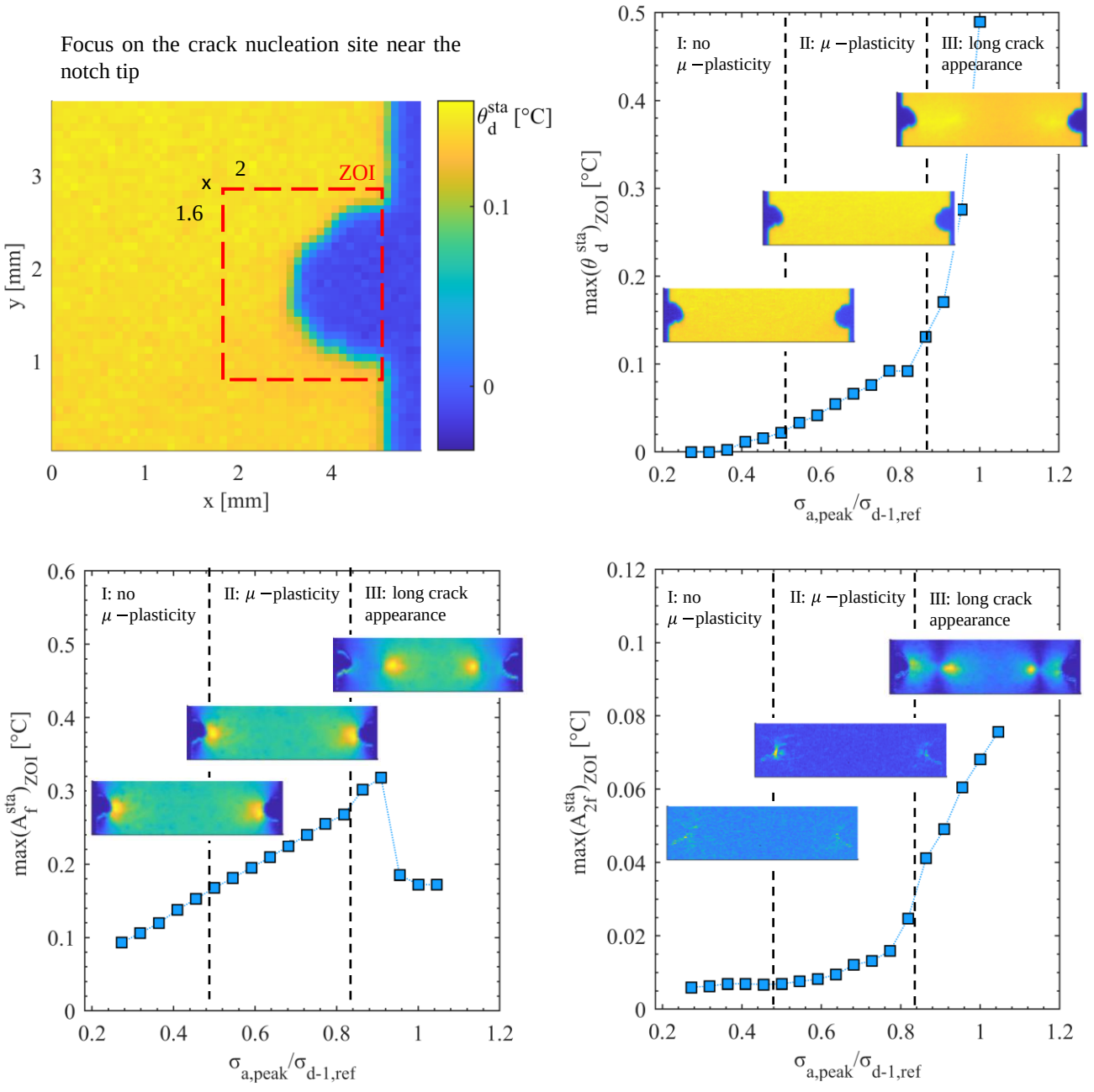

Fig. 11. The evolutions of θ_d^{sta}, A_f^{sta} and A_{2f}^{sta} maximum values inside the ZOI for as-built L-PBF Ti-6Al-4V during uniaxial fatigue test (R = -1) at a load frequency of 30Hz.

The results obtained from the fatigue test allow for the estimation of a microplasticity threshold [33,34,62], which is considered as the fatigue limit in this study. To determine the microplasticity threshold, the intersection of the slopes defined by data points in the first stage I and the second stage II of the evolution plots (θ_d^{sta} and A_{2f}^{sta}) is identified. This method, although debatable, provides a straightforward way to

estimate the microplasticity threshold. Similar approaches have been used in previous studies on Ti-6Al-4V [41]. It is important to note that the choice of the data points to extract the slopes is subject to discussion and may introduce some variability in the results. In Fig. 12, an example of the estimated fatigue limits extracted using this method is provided. The evolution of A_{2f}^{sta} is particularly representative of the thermal dissipation in the material. However, it should be noted that the temperature levels in the L-PBF Ti-6Al-4V material are relatively low due to its lower thermal conductivity compared to steel. On the other hand, θ_d^{sta} is more sensible to surrounding noise, which is also a consequence to the choice to retrieve the maximum value and not the average other pixels within the ZOI.

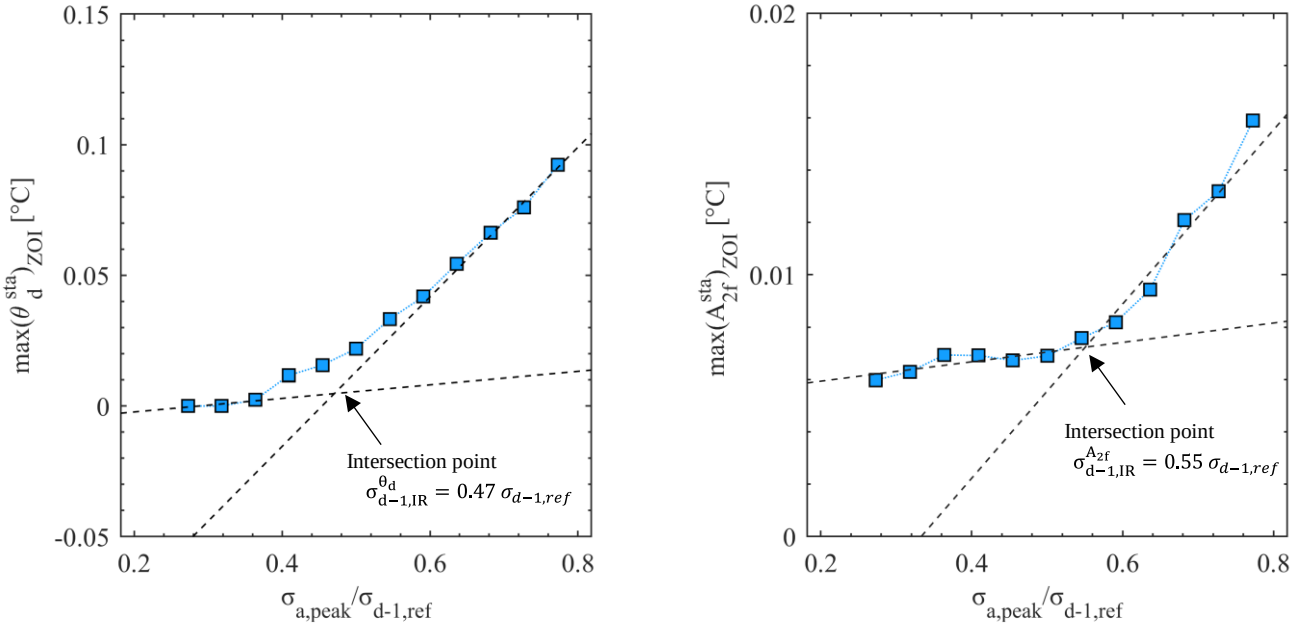

Fig. 12. Example of fatigue limit estimation using $\max(\theta_d^{sta})_{ZOI}$ and $\max(A_{2f}^{sta})_{ZOI}$ evolutions for as-built L-PBF Ti-6Al-4V.

3. Results

In this section, we will present the results obtained from both the staircase procedure and the thermographic method. The analysis is divided into two parts: the effects of surface treatments and the effects of heat treatments.

3.1. Effect of surface treatments

This section focuses on the evaluation of the surface treatments influence on the HCF strength of stress-relieved L-PBF Ti-6Al-4V specimens. The obtained results from the thermographic method are compared to the SN curves (*cf.* Fig. 13). The Palmgren formulism, see eq. (8), is used to extrapolate the stress amplitude according to the number of cycles. For confidentiality reasons, the fatigue limits are normalized according to the reference material fatigue limit determined by the staircase method, results are presented in Table 6.

$$\sigma_a = \sigma_{d-1} + \left(\frac{C}{A+N}\right)^{\frac{1}{b}} \quad (8)$$

Results obtained following the Dixon and Mood [55] staircase methodology are resumed in Table 6. The stress steps had to be adjusted according to the surface state. Dixon and Mood statistics criteria were validated for each material configuration except for the as-built surface state, the chosen stress step was too high. Higher surface roughness tends to decrease the scattering as the lowest standard deviations are obtained for the as-built and blasted L-PBF Ti-6Al-4V. The fatigue limit of the as-built surface state is significantly lower, 50% below the fatigue limit of the reference material. This substantial difference highlights the existing disparity between AM and conventional manufacturing processes. However, the raw performance

can be greatly enhanced through the application of blasting treatment. In fact, the fatigue limit is increased by 50%, indicating a significant improvement considering the simplicity of the treatment. Furthermore, the fatigue limit achieved with chemical etching treatment closely approaches 0.7 $\sigma_{d-1,ref}$ which corresponds to a 60% enhancement. In terms of feasibility, achieving better results would be challenging as the process only requires immersing the part in a chemical solution and monitoring the immersion time. Surprisingly, the machined L-PBF Ti-6Al-4V specimens exhibited a similar fatigue limit to that of the reference Ti-6Al-4V, which is an intriguing finding considering the presence of porosity defects. The highest fatigue limit was observed in the specimens subjected to chemical etching, followed by blasting treatment. This result cannot be solely attributed to surface roughness since it surpasses that of the machined specimens and matches the surface roughness of the chemically etched ones. The only plausible explanation lies in the difference in the surface layer condition, specifically the presence of compressive stresses that have a beneficial effect.

Table 6. Overview of fatigue limits and standard deviations determined at 10^7 cycles using the staircase method.

Material configuration	Initial stress $\sigma_{a,peak_0}/\sigma_{d-1,ref}$	Stress step d [MPa]	Number of tested specimens N_b	Fatigue limit at 10^7 cycles $\sigma_{d-1,str}/\sigma_{d-1,ref}$	Standard deviation [MPa]
AM Ti64 AB	0.43	15	11	0.45	<15
AM Ti64 Blasted	0.63	15	11	0.67	10
AM Ti64 CE	0.71	15	14	0.73	27
AM Ti64 CE & Blasted	1.00	30	11	1.05	33
AM Ti64 Machined	0.95	15	9	1.00	17
Ref Ti64	0.97	30	12	1.00	29

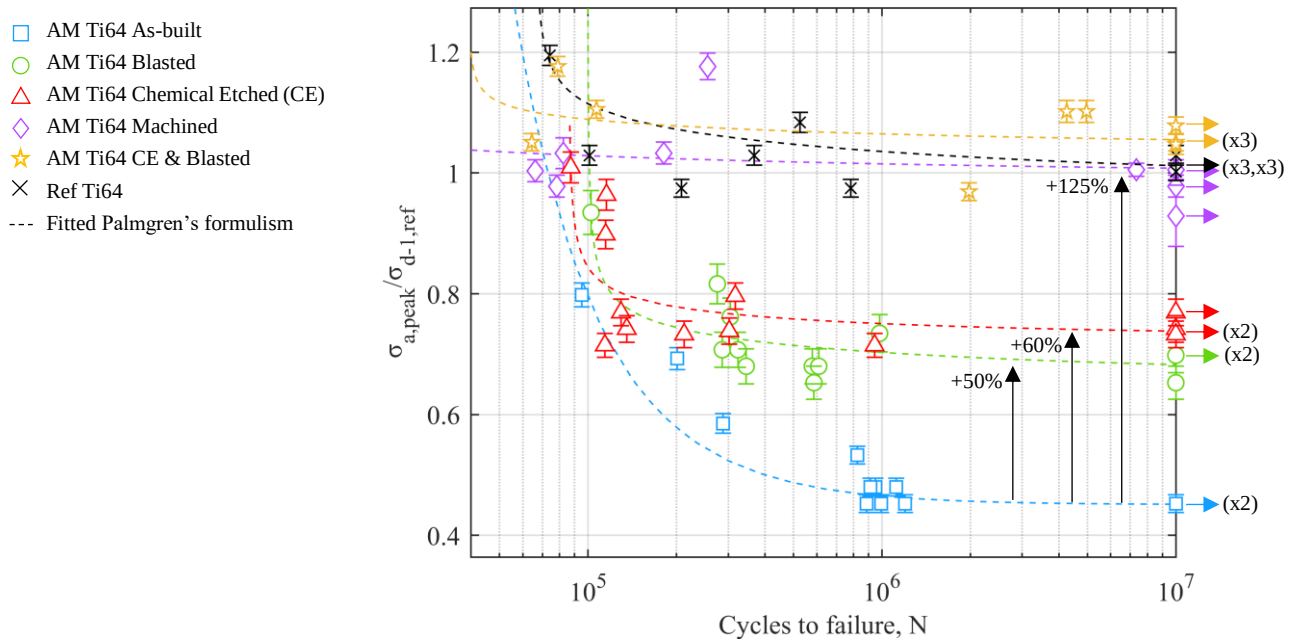

Fig. 13. S-N curves comparing L-PBF Ti-6Al-4V with varying surface states and ref Ti-6Al-4V obtained from uniaxial fatigue tests (R = -1) conducted at a load frequency of 40 Hz, using the laboratory C-notched specimen design.

Results obtained with thermographic method are now discussed beginning with the evolution of A_f^{sta}. It is observed that A_f^{sta} increases proportionally with the stress amplitude, as defined by equation (8) which relates to thermoelastic stress analysis (TSA) [63]. The stress field can be determined from the A_f^{sta} temperature values, but here values differ between different surface states (*cf.* Fig. 14). It can be attributed to variations in the initial temperature T_0, see equation (8).

$$A_f = \frac{\alpha_k T_0 \dot{\bar{\bar{\sigma}}}}{\rho C_p} \quad (8)$$

With α_k is the material expansion coefficient factor, $\dot{\bar{\bar{\sigma}}}$ the derived stress tensor, ρ the material density and C_p the material specific heat.

Additionally, the measured temperature levels are quite low due to the properties of the material and the stress concentration factor K_t induced by the notch, resulting in a highly stressed surface. Moreover, different surface roughness can locally modify the stress and it explains the use of the maximum value, *i.e.*, pixel size value, rather than the conventional average value over the ZOI. These factors make the results more sensitive to temperature variations in the surrounding environment.

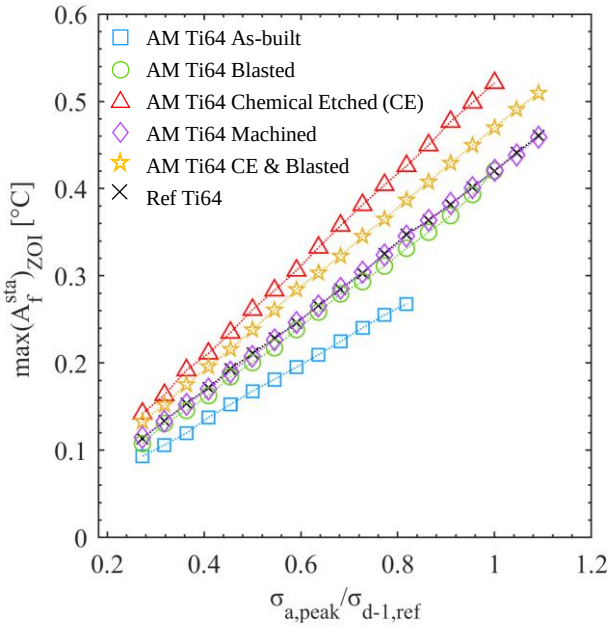

Fig. 14. The evolutions of A_f^{sta} maximum values over the ZOI obtained with infrared thermographic method during uniaxial fatigue tests (R = -1) at a load frequency of 30 Hz for L-PBF and reference Ti-6Al-4V.

The evolutions of A_{2f}^{sta} (*cf.* Fig. 15) and θ_d^{sta} (*cf.* Fig. 16) are presented in two separate figures due to the emergence of distinct trends: rougher surface finish and smoother surface finish. In the case of the as-built, blasted, and chemical etched specimens, higher thermal dissipation is observed as A_{2f}^{sta} increases at lower stress levels (left of Fig. 15). Similar observations can be made regarding the behavior of θ_d^{sta} (left of Fig. 16) except for the chemical etched material, which exhibits a temperature drop at 0.7 $\sigma_{d-1,ref}$. This unexpected drop could potentially be attributed to surrounding temperature noise, as it is not seen in A_{2f}^{sta} evolution. It should be noted that a linear regression is applied to subtract the initial levels from θ_d^{sta} to ensure a better comparison between each surface treatment, as the initial temperature levels were not identical. Additionally, the last data points belonging to stage III, as defined in Fig. 11 when a long crack appears, have been removed from the analysis. When comparing the rougher surface finish, the behaviors are quite similar during stage I but in stage II slopes are different. The as-built specimen exhibits a steeper increase compared to the blasted and chemical etched specimens. Furthermore, the long crack appears earlier in the as-built surface finish material.

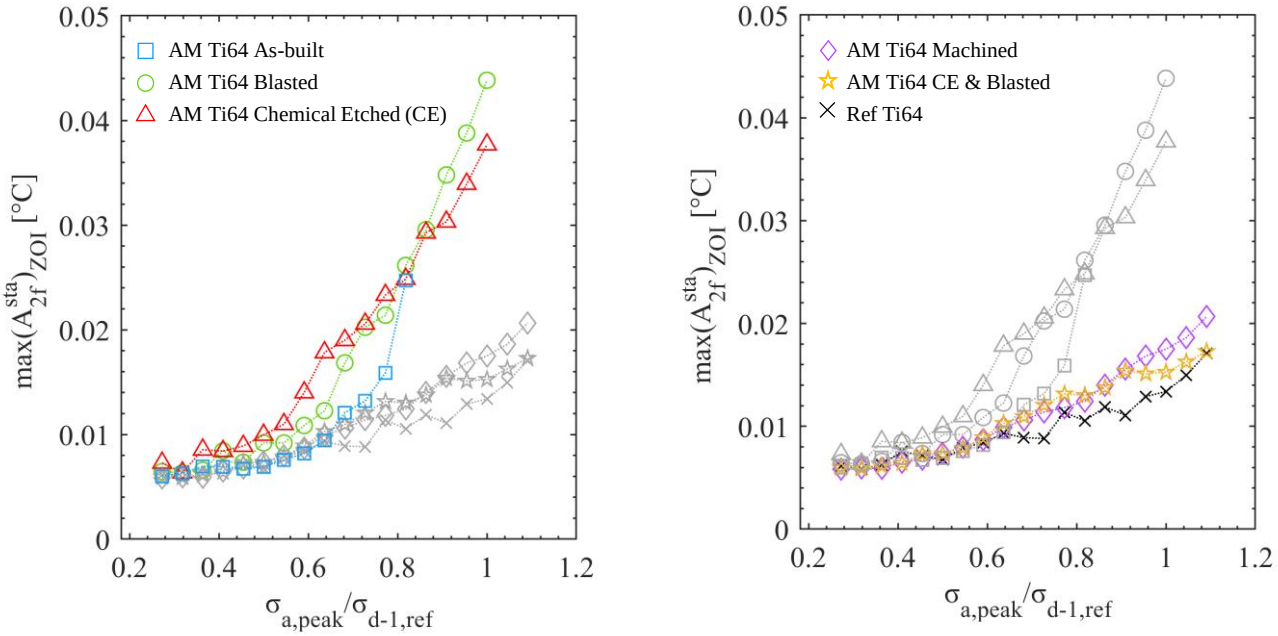

Fig. 15. The evolutions of A_{2f}^{sta} maximum values obtained with infrared thermographic method during uniaxial fatigue tests (R = -1) for L-PBF Ti-6Al-4V with rougher surface state on left and smoother surface state on right.

The results of machined L-PBF Ti-6Al-4V, machined cast Ti-6Al-4V and the L-PBF Ti-6Al-4V that underwent chemical etching followed by ceramic microbeads blasting (CE & blasted) are presented in both right of Fig. 15 for A_{2f}^{sta}, and Fig. 16 for θ_d^{sta}.When examining the evolutions of θ_d^{sta} and A_{2f}^{sta}, the behaviors are very similar across different surface states, making it challenging to establish a distinct order. However, when comparing θ_d^{sta} and A_{2f}^{sta} it becomes evident that θ_d^{sta} data is more scattered and more susceptible to noise, whereas the evolutions of A_{2f}^{sta} are smoother, but temperature levels are very low (<0.05°C).

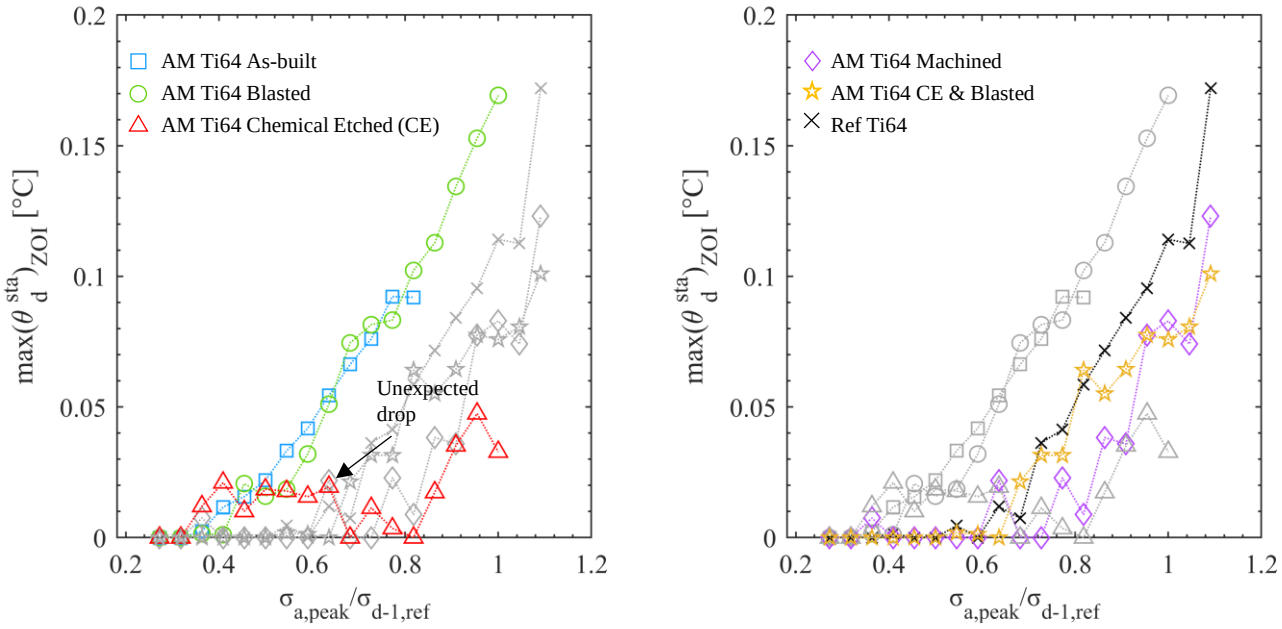

Fig. 16. The evolutions of θ_d^{sta} maximum values obtained with infrared thermographic method during uniaxial fatigue tests (R = -1) for L-PBF Ti-6Al-4V with rougher surface state on left and smoother surface state on right.

Table 7 presents the estimated fatigue limits obtained using the slope method, as discussed in the previous sections, and compares them to the fatigue limits obtained through the staircase method. The

estimated fatigue limit $\sigma_{d-1,IR}$ using the infrared thermographic method is defined as the average of the estimated fatigue limits obtained from θ_d^{sta} and A_{2f}^{sta}:

$$\sigma_{d-1,IR} = \frac{\sigma_{d-1,\theta_d^{sta}} + \sigma_{d-1,A_{2f}^{sta}}}{2} \quad (9)$$

The relative errors of the estimated fatigue limits via infrared thermographic method are defined as follows:

$$\%Err = \frac{\left|\sigma_{d-1,IR} - \sigma_{d-1,str}\right|}{\sigma_{d-1,str}} * 100 \quad (10)$$

The errors are reasonable and comparable between each material, however the error is a bit higher for the rougher surface state, i.e. the as-built configuration. As is evident from Fig. 17, the predicted fatigue limits ($\sigma_{d-1,IR}$) closely align with the estimated fatigue limits obtained via the staircase procedure ($\sigma_{d-1,str}$) thus attesting to the validity and reliability of the infrared thermographic method to estimate the fatigue limits.

.

Table 7. Fatigue limits of L-PBF and ref Ti-6Al-4V obtained via staircase method and the infrared thermographic method.

Specimen configuration	$\sigma_{d-1,\theta_d^{sta}}/\sigma_{d-1,ref}$	$\sigma_{d-1,A_{2f}^{sta}}/\sigma_{d-1,ref}$	$\sigma_{d-1,IR}/\sigma_{d-1,ref}$	$\sigma_{d-1,str}/\sigma_{d-1,ref}$	%Err θ_d^{sta}	%Err A_{2f}^{sta}	%Err $\sigma_{d-1,IR}$
AM Ti64 AB (as-built)	0.47	0.55	0.51	0.45	6%	24%	15%
AM Ti64 Blasted	0.65	0.65	0.65	0.67	1%	1%	1%
AM Ti64 Chemical Etched (CE)	0.81	0.69	0.75	0.73	12%	4%	4%
AM Ti64 CE & Blasted	0.89	0.97	0.93	1.05	15%	8%	11%
AM Ti64 Machined	0.97	0.94	0.95	1.00	3%	7%	5%
Ref Ti64	0.95	0.94	0.95	1.00	4%	5%	5%

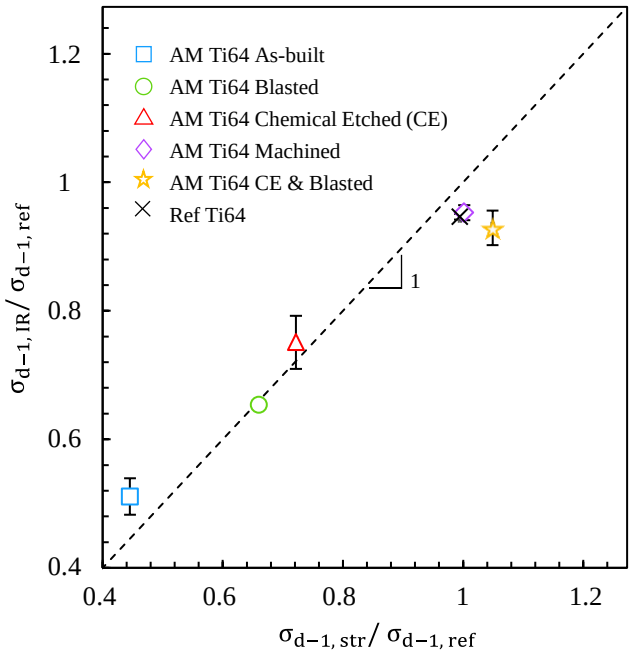

Fig. 17. Estimated fatigue limits from IR thermographic method $\sigma_{d-1,IR}$ according to determined fatigue limits with staircase method $\sigma_{d-1,str}$.

3.2. Microstructure effect

Considering that the infrared thermographic technique yields to results close to the fatigue limits determined by the staircase method, further experiments were conducted on heat-treated materials to investigate the effect of microstructure. Tests were performed on blasted L-PBF Ti-6Al-4V specimens with the three heat treatments described in Table 4 as well as on machined L-PBF Ti-6Al-4V. The evolutions of A_{2f}^{sta} are analyzed for this comparison (*cf*. Fig. 18).

Two distinct behaviors were observed: higher thermal dissipation for the blasted surface state compared to the machined surface state, indicating the influence of surface roughness. However, when comparing the different heat treatments (represented by different color schemes), the behaviors were found to be quite similar, and no potential enhancement or reduction in fatigue strength could be identified. This finding was significant, as there was hope to observe a beneficial impact of the sub-transus heat treatment. Based on these trends, a decision was made not to conduct a staircase-type procedure on the microstructures resulting from the sub-transus and super-transus heat treatments, as their potential for enhancing fatigue performance appears to be limited.

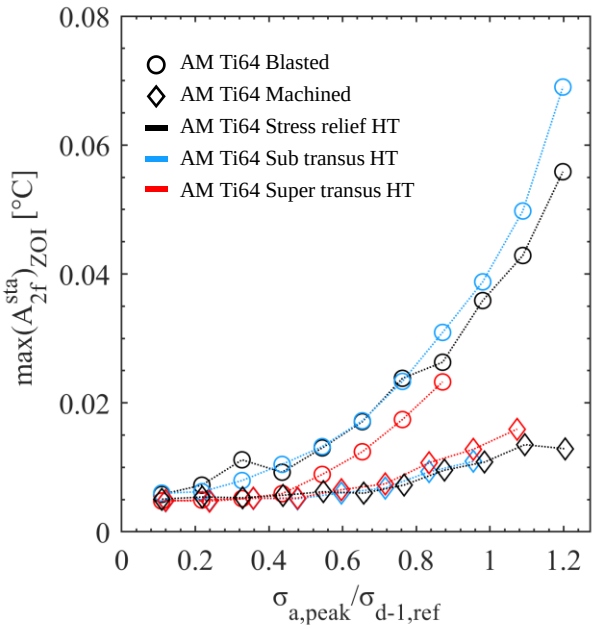

Fig. 18. The evolutions of A_{2f}^{sta} maximum values obtained with infrared thermographic method during fully reversed uniaxial fatigue test (R = -1) for blasted and machined L-PBF Ti-6Al-4V with stress relief, sub-transus and super-transus heat treatments.

4. Discussion

4.1. Stress gradient or size effect

This work highlights the influence of surface treatments on the fatigue performance of AM L-PBF Ti-6Al-4V under the presence of a stress gradient. It was crucial to replicate the stress gradient to closely resemble the conditions experienced in industrial applications, as it is known to have a significant impact on fatigue behavior.

Comparing the fatigue limit of the AM machined specimens with the reference Ti-6Al-4V, equivalent fatigue limits are observed. This result is interesting considering that the surface states are relatively similar, but the AM alloy contains internal porosity defects, which would typically result in a lower fatigue limit. However, when hot isostatic pressure (HIP) treatment is applied to the AM material, effectively suppressing or significantly reducing porosity through a conventional cylindrical specimen design, equivalent fatigue strength is achieved [12,64]. In cases where the AM material is not subjected to HIP treatment and exhibits a machined surface state, fatigue failure often originates from a porosity defect, leading to premature failure. The particularity of this study is that fatigue tests were conducted on a notched design with a significant stress gradient. Consequently, the impact of porosity defects on fatigue strength is greatly diminished due to the stress gradient effect, which concentrates the stress in a small volume compared to the entire part. Therefore, the likelihood of crack nucleation from an internal defect is directly linked to the probability of encountering

a porosity defect within this specific volume. It is worth noting that when the surface roughness is sufficiently high, cracks tend to nucleate from surface defects. This is observed in the as-built, blasted, and chemical etched surface states. However, in the case of machining, cracks primarily nucleate from the surface, but nucleation from internal defects near the free surface is also observed. This result is significant as it reduces the scatter commonly encountered when dealing with AM materials due to the presence of inherent defects. Thus, the surface roughness in the presence of a stress gradient is the most important parameter regarding the fatigue limit.

4.2. Residual stresses impact

Among the different material configurations studied, two configurations potentially exhibit compressive stresses as a result of the surface treatment: AM Ti-6Al-4V with a blasted surface state and chemical etching followed by blasting. However, this work does not provide clear evidence of the influence of compressive stresses on the material with the blasted surface state. In contrast, for the chemical etched followed by blasting surface state, the addition of the blasting treatment positively impacts the fatigue limit. Surface roughness analysis revealed equivalent S_a and S_v values for the materials treated with chemical etching alone and with chemical etching followed by blasting. However, the fatigue limit is 40% higher when the blasting treatment is included. Surprisingly, the performance of this material configuration surpasses that of the reference material and AM Ti-6Al-4V with a machined surface state, despite the remaining poor surface roughness. The explanation for this unexpected result may lie in the depth of the induced compressive stresses, which is sufficiently large to counteract the negative impact of surface roughness.

To address this matter, a quantitative evaluation of residual stresses was performed using X-ray diffraction measurements conducted by MELIAD company. These measurements followed the NF EN 15305 standard, and each measurement point is an average over a 5µm depth. The main focus was on the load direction (z-axis), aligned with the material's build direction. Multiple measurements were taken at specific depths with a consistent 25µm interval. Chemical etching was utilized to remove material along the depth, avoiding the introduction of residual stresses linked to machining procedures. A reference specimen (AM Ti64 CE), without the blasting step, was used as a standard for comparison. A single measurement was conducted at the surface in the horizontal direction (x-axis). The results are presented in Fig. 19 and confirms the presence of compressive stresses. Note that the results were divided by the reference Ti-6Al-4V fatigue strength.

On the reference sample, residual stresses are close zero in both vertical, -0.08 $\sigma_{d-1,ref}$ MPa (σ_{zz}), and horizontal, -0.04 $\sigma_{d-1,ref}$ MPa horizontally (σ_{xx}), directions. This attests that the relief heat treatment facilitates the relaxation of residual stresses induced by the AM process. In contrast, the blasting treatment introduces substantial compressive stresses. At the surface, residual stresses of -1.5 $\sigma_{d-1,ref}$ vertically and -1.3 $\sigma_{d-1,ref}$ horizontally are evaluated. The residual stresses σ_{zz}, aligned with both the build and load directions, diminish to -0.24 $\sigma_{d-1,ref}$ at 50 µm, thereafter stabilizing up to a depth of. This level of compressive stresses aligns with findings from related literature using blasting with comparable abrasive media, specifically ceramic micro-beads, on titanium alloys [50,65].

Consequently, the marked enhancement in fatigue strength with this specific surface treatment can be attributed to the presence of compressive stresses at the surface, as imagined. The penetration depth of compressive stresses reaches 50 µm, with a value from -1.5 $\sigma_{d-1,ref}$ to -0.24 $\sigma_{d-1,ref}$. In comparison with the maximum pit depth ($S_v = 31.2$ µm) it underscores that compressive stresses can mitigate the detrimental effect of surface roughness. The beneficial impact of compressive stresses on fatigue strength is further amplified by the presence of the stress gradient which induces a highly stressed volume, thereby mitigating the adverse effect of porosity defects.

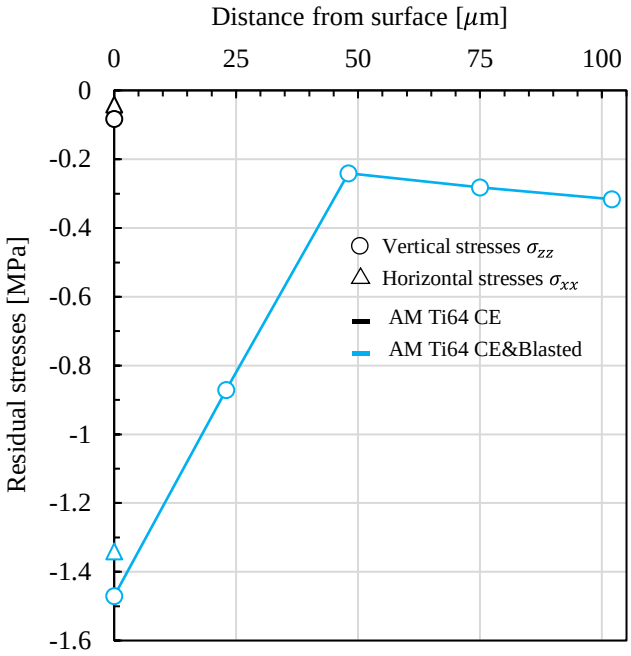

Fig. 19. The residual stresses measurements with X-ray diffraction in horizontal and vertical directions for AM Ti-6Al-4V with blasting (blue) and without (black) according to the distance from the surface.

4.3. Interest of the infrared thermographic method

The infrared thermographic method was employed to assess the potential beneficial impact of post-processing treatments on fatigue strength, allowing for the selection of a few treatments to undergo the more time-consuming staircase procedure. By measuring the material heat using an infrared camera during the fatigue test and the post-treatment described earlier in this article, microplasticity thresholds were identified, which we consider as the fatigue limit. This semi-quantitative method offers the advantage of providing results quickly, as a single test can be sufficient. Note that for this study it was the maximum pixel values within the ZOI that were used instead of the average pixel's values. The pixel size (0.08mm/x) is then a key parameter, it is equivalent to S_v value for the as-built surface state configuration. Therefore, this could explain why the error is higher for this one compared to the smoother surface state, for a better accuracy the IR camera resolution could be improved.

The estimated fatigue limits obtained through the infrared thermographic method closely align with those determined using the staircase procedure, as observed in Fig. 17. However, the main challenge encountered was related to the stress gradient effect, which localizes the stresses and consequently the heat dissipation, and the high surface roughness. Additionally, the temperature levels recorded during the tests were very low due to the low material heat conductivity and the presence of the stress gradient.

4.4. Microstructure role

Fatigue tests using the infrared thermographic method were conducted on materials with different microstructures to investigate their potential impact on fatigue strength. Conventional heat treatments for Ti-6Al-4V were applied with two surface treatments: blasting and machining. These heat treatments resulted in different macroscopic microstructures, with elongated columnar prior β grains transforming into equiaxed grains with super-transus heat treatment. At the microscale, the appearance of α lamellae was observed with the sub-transus heat treatment.

Despite the variations in microstructure, the A_f^{sta} evolutions for the different microstructures were found to be very similar, making it difficult to discern any potential effect on fatigue strength. In the case of the blasting surface treatment, where the surface roughness is high, fatigue failure is primarily governed by surface defects. Therefore, it is not surprising that no significant effect of the microstructure was observed.

Even when the specimens were machined, no major differences in behavior were noticeable. This leads to the assumption that the influence of microstructure is not significant enough to be captured by the thermographic method, or that the effects of porosity and surface defects outweigh any potential influence of the microstructure.

5. Conclusion

Additive manufacturing is a promising technology for the production of complex-shaped mechanical parts. However, it is important to address the challenges associated with the fatigue strength of additive manufactured components. This study focused on investigating the influence of post-processing treatments on the fatigue performance of Ti-6Al-4V, a commonly used titanium alloy, under a stress gradient inspired by an industrial component, the coupling.

Numerical tools, such as finite element analysis, were employed to characterize the multi-axial stress state and the hydrostatic stress gradient in the coupling. Additionally, an infrared thermographic method was utilized to quickly compare the effects of selected post-processing treatments on the fatigue strength, avoiding the need for expensive and time-consuming fatigue tests. Fatigue tests respecting the staircase procedure were conducted on the treatments that showed the most potential for fatigue limit enhancement.

The findings of this study can be summarized as follows:

- The infrared thermographic method proved to be a useful tool for quickly evaluating the influence of selected treatments on fatigue performance. While it has been effective for steels in previous studies, the presence of a stress gradient in titanium alloy made it more challenging to capture thermal dissipation accurately like in [35,66]. Nevertheless, the method provided general trends similar to the staircase procedure and yielded satisfactory estimated fatigue limits.
- Surface treatments, specifically blasting and chemical etching, were found to significantly reduce surface roughness and enhance fatigue strength. Chemical etching, in particular, demonstrated superior performance and ease of application to complex structures. However, it should be noted that chemical etching removes material, which needs to be considered during the design process. The addition of blasting after chemical etching further improved performance by introducing compressive stresses. While more challenging to apply to all areas of a part, the combination of chemical etching and blasting yielded considerably better results. The choice between these treatments depends on the desired level of fatigue strength, with chemical etching being suitable for moderate improvements and the addition of blasting for higher performance.
- The stress gradient effect was found to be highly significant. It accentuated crack nucleation from surface defects rather than porosity defects and contributed to reducing scattering in fatigue failure. This finding suggests that fatigue failure prediction models should focus on capturing this particular feature if the mechanical component exhibits a stress gradient.

Overall, this work highlights the importance of post-processing treatments in improving the fatigue strength of additive manufactured Ti-6Al-4V under a stress gradient. The findings provide valuable insights for optimizing post-processing strategies and designing fatigue-resistant components. Further research could focus on refining the infrared thermographic method for better evaluation of thermal dissipation in the presence of high stress gradients and exploring additional post-processing techniques to enhance fatigue performance.

Acknowledgements

The authors would like to express their gratitude to John Crane for its financial and scientific support. The authors also extend their appreciation to the Association Nationale de la Recherche et de la Technologie (ANRT) for funding this project.

References

[1] T.D. Ngo, A. Kashani, G. Imbalzano, K.T.Q. Nguyen, D. Hui, Additive manufacturing (3D printing): A review of materials, methods, applications and challenges, Compos. Part B Eng. 143 (2018) 172–196. https://doi.org/10.1016/j.compositesb.2018.02.012.

[2] W.E. Frazier, Metal additive manufacturing: A review, J. Mater. Eng. Perform. 23 (2014) 1917–1928. https://doi.org/10.1007/s11665-014-0958-z.

[3] D. Herzog, V. Seyda, E. Wycisk, C. Emmelmann, Additive manufacturing of metals, Acta Mater. 117 (2016) 371–392. https://doi.org/10.1016/j.actamat.2016.07.019.

[4] T. DebRoy, H.L. Wei, J.S. Zuback, T. Mukherjee, J.W. Elmer, J.O. Milewski, A.M. Beese, A. Wilson-Heid, A. De, W. Zhang, Additive manufacturing of metallic components – Process, structure and properties, Prog. Mater. Sci. 92 (2018) 112–224. https://doi.org/10.1016/j.pmatsci.2017.10.001.

[5] N. Sanaei, A. Fatemi, N. Phan, Defect characteristics and analysis of their variability in metal L-PBF additive manufacturing, Mater. Des. 182 (2019) 108091. https://doi.org/10.1016/j.matdes.2019.108091.

[6] S. Liu, Y.C. Shin, Additive manufacturing of Ti6Al4V alloy: A review, Mater. Des. 164 (2019) 107552. https://doi.org/10.1016/j.matdes.2018.107552.

[7] H. Gong, K. Rafi, H. Gu, T. Starr, B. Stucker, Analysis of defect generation in Ti-6Al-4V parts made using powder bed fusion additive manufacturing processes, Addit. Manuf. 1 (2014) 87–98. https://doi.org/10.1016/j.addma.2014.08.002.

[8] J.W. Pegues, S. Shao, N. Shamsaei, N. Sanaei, A. Fatemi, D.H. Warner, P. Li, N. Phan, Fatigue of additive manufactured Ti-6Al-4V, Part I: The effects of powder feedstock, manufacturing, and post-process conditions on the resulting microstructure and defects, Int. J. Fatigue. 132 (2020). https://doi.org/10.1016/j.ijfatigue.2019.105358.

[9] D. Novovic, R.C. Dewes, D.K. Aspinwall, W. Voice, P. Bowen, The effect of machined topography and integrity on fatigue life, Int. J. Mach. Tools Manuf. 44 (2004) 125–134. https://doi.org/10.1016/j.ijmachtools.2003.10.018.

[10] N. Sanaei, A. Fatemi, Analysis of the effect of surface roughness on fatigue performance of powder bed fusion additive manufactured metals, Theor. Appl. Fract. Mech. (2020).

[11] A. Fatemi, R. Molaei, S. Sharifimehr, N. Shamsaei, N. Phan, Torsional fatigue behavior of wrought and additive manufactured Ti-6Al-4V by powder bed fusion including surface finish effect, Int. J. Fatigue. 99 (2017) 187–201. https://doi.org/10.1016/j.ijfatigue.2017.03.002.

[12] H. Masuo, Y. Tanaka, S. Morokoshi, H. Yagura, T. Uchida, Y. Yamamoto, Y. Murakami, Influence of defects, surface roughness and HIP on the fatigue strength of Ti-6Al-4V manufactured by additive manufacturing, Int. J. Fatigue. 117 (2018) 163–179. https://doi.org/10.1016/j.ijfatigue.2018.07.020.

[13] B. Vayssette, N. Saintier, C. Brugger, M. Elmay, E. Pessard, Surface roughness of Ti-6Al-4V parts obtained by SLM and EBM: Effect on the High Cycle Fatigue life, Procedia Eng. 213 (2018) 89–97. https://doi.org/10.1016/j.proeng.2018.02.010.

[14] Y. Murakami, T. Endo, Effects of small defects on fatigue strength of metals, Int. J. Fatigue. 2 (1980) 23–30. https://doi.org/10.1016/0142-1123(80)90024-9.

[15] Y. Murakami, M. Endo, Effects of defects, inclusions and inhomogeneities on fatigue strength, Int. J. Fatigue. 16 (1994) 163–182. https://doi.org/10.1016/0142-1123(94)90001-9.

[16] B. Vayssette, N. Saintier, C. Brugger, M. El May, E. Pessard, Numerical modelling of surface roughness effect on the fatigue behavior of Ti-6Al-4V obtained by additive manufacturing, Int. J.

Fatigue. 123 (2019) 180–195. https://doi.org/10.1016/j.ijfatigue.2019.02.014.

[17] N. Sanaei, A. Fatemi, Defects in additive manufactured metals and their effect on fatigue performance: A state-of-the-art review, Prog. Mater. Sci. 117 (2021) 100724. https://doi.org/10.1016/j.pmatsci.2020.100724.

[18] Y.N. Hu, S.C. Wu, P.J. Withers, J. Zhang, H.Y.X. Bao, Y.N. Fu, G.Z. Kang, The effect of manufacturing defects on the fatigue life of selective laser melted Ti-6Al-4V structures, Mater. Des. 192 (2020). https://doi.org/10.1016/j.matdes.2020.108708.

[19] I. Koutiri, D. Bellett, F. Morel, E. Pessard, A probabilistic model for the high cycle fatigue behaviour of cast aluminium alloys subject to complex loads, Int. J. Fatigue. 47 (2013) 137–147. https://doi.org/10.1016/j.ijfatigue.2012.08.004.

[20] I. Serrano-Munoz, J.Y. Buffiere, C. Verdu, Y. Gaillard, P. Mu, Y. Nadot, Influence of surface and internal casting defects on the fatigue behaviour of A357-T6 cast aluminium alloy, Int. J. Fatigue. 82 (2016) 361–370. https://doi.org/10.1016/j.ijfatigue.2015.07.032.

[21] P. Mu, Y. Nadot, C. Nadot-Martin, A. Chabod, I. Serrano-Munoz, C. Verdu, Influence of casting defects on the fatigue behavior of cast aluminum AS7G06-T6, Int. J. Fatigue. 63 (2014) 97–109. https://doi.org/10.1016/j.ijfatigue.2014.01.011.

[22] W. Weibull, A statistical distribution function of wide applicability, J. Appl. Mech. (1951).

[23] E. Pessard, F. Morel, A. Morel, D. Bellett, Modelling the role of non-metallic inclusions on the anisotropic fatigue behaviour of forged steel, Int. J. Fatigue. 33 (2011) 568–577. https://doi.org/10.1016/j.ijfatigue.2010.10.012.

[24] E. Pessard, M. Lavialle, P. Laheurte, P. Didier, M. Brochu, High-cycle fatigue behavior of a laser powder bed fusion additive manufactured Ti-6Al-4V titanium: Effect of pores and tested volume size, Int. J. Fatigue. 149 (2021) 106206. https://doi.org/10.1016/j.ijfatigue.2021.106206.

[25] H.K. Rafi, N. V. Karthik, H. Gong, T.L. Starr, B.E. Stucker, Microstructures and mechanical properties of Ti6Al4V parts fabricated by selective laser melting and electron beam melting, J. Mater. Eng. Perform. 22 (2013) 3872–3883. https://doi.org/10.1007/s11665-013-0658-0.

[26] A.A. Antonysamy, J. Meyer, P.B. Prangnell, Effect of build geometry on the β-grain structure and texture in additive manufacture of Ti6Al4V by selective electron beam melting, Mater. Charact. 84 (2013) 153–168. https://doi.org/10.1016/j.matchar.2013.07.012.

[27] J.A. Hall, Fatigue crack initiation in alpha-beta titanium alloys, Int. J. Fatigue. 19 (1997) 23–37. https://doi.org/10.1016/s0142-1123(97)00047-9.

[28] I. V. Papadopoulos, V.P. Panoskaltsis, Invariant formulation of a gradient dependent multiaxial high-cycle fatigue criterion, Eng. Fract. Mech. 55 (1996) 513–528. https://doi.org/10.1016/S0013-7944(96)00047-1.

[29] R. Molaei, A. Fatemi, N. Sanaei, J. Pegues, N. Shamsaei, S. Shao, P. Li, D.H. Warner, N. Phan, Fatigue of additive manufactured Ti-6Al-4V, Part II: The relationship between microstructure, material cyclic properties, and component performance, Int. J. Fatigue. 132 (2020). https://doi.org/10.1016/j.ijfatigue.2019.105363.

[30] A. Soltani-Tehrani, M. Habibnejad-Korayem, S. Shao, M. Haghshenas, N. Shamsaei, Ti-6Al-4V Powder Characteristics in Laser Powder Bed Fusion: The Effect on Tensile and Fatigue Behavior, Addit. Manuf. 51 (2021) 102584. https://doi.org/10.1016/j.addma.2021.102584.

[31] M.P. Luong, Fatigue limit evaluation of metals using an infrared thermographic technique, Mech. Mater. 28 (1998) 155–163. https://doi.org/10.1016/S0167-6636(97)00047-1.

[32] H.F. Moore, J.B. Kommers, Fatigue of metals under repeated stress, Chem. Metall. Eng. 25 (1921) 1141–1144.

[33] G. La Rosa, A. Risitano, Thermographic methodology for rapid determination of the fatigue limit of materials and mechanical components, Int. J. Fatigue. 22 (2000) 65–73. https://doi.org/10.1016/S0142-1123(99)00088-2.

[34] C. Doudard, M. Poncelet, S. Calloch, C. Boue, F. Hild, A. Galtier, Determination of an HCF criterion by thermal measurements under biaxial cyclic loading, Int. J. Fatigue. 29 (2007) 748–757. https://doi.org/10.1016/j.ijfatigue.2006.06.009.

[35] A.R. Moustafa, B. Berthel, S. Fouvry, E. Charkaluk, Quantitative calorimetric analysis of the fretting damage: Construction of the elastic shakedown boundary, Int. J. Fatigue. 95 (2017) 143–155. https://doi.org/10.1016/j.ijfatigue.2016.10.018.

[36] C. Douellou, X. Balandraud, E. Duc, B. Verquin, F. Lefebvre, F. Sar, Rapid characterization of the fatigue limit of additive-manufactured maraging steels using infrared measurements, Addit. Manuf. 35 (2020). https://doi.org/10.1016/j.addma.2020.101310.

[37] P. Bayati, A. Jahadakbar, M. Barati, M. Nematollahi, L. Saint-Sulpice, M. Haghshenas, S.A. Chirani, M.J. Mahtabi, M. Elahinia, Toward low and high cycle fatigue behavior of SLM-fabricated NiTi: Considering the effect of build orientation and employing a self-heating approach, Int. J. Mech. Sci. 185 (2020). https://doi.org/10.1016/j.ijmecsci.2020.105878.

[38] Y. Cao, Z. Moumni, J. Zhu, Y. Zhang, Y. You, W. Zhang, Comparative investigation of the fatigue limit of additive-manufactured and rolled 316 steel based on self-heating approach, Eng. Fract. Mech. 223 (2020). https://doi.org/10.1016/j.engfracmech.2019.106746.

[39] C. Colombo, A. Tridello, A.P. Pagnoncelli, C.A. Biffi, J. Fiocchi, A. Tuissi, L.M. Vergani, D.S. Paolino, Efficient experimental methods for rapid fatigue life estimation of additive manufactured elements, Int. J. Fatigue. 167 (2023). https://doi.org/10.1016/j.ijfatigue.2022.107345.

[40] V. Roué, C. Doudard, S. Calloch, F. Montel, Q. Pujol D'Andrebo, F. Corpace, Rapid determination of the high cycle fatigue properties of high temperature aeronautical alloys by self-heating measurements, MATEC Web Conf. 165 (2018) 1–9. https://doi.org/10.1051/matecconf/201816522022.

[41] A. Akai, D. Shiozawa, T. Sakagami, Fatigue limit estimation of titanium alloy Ti-6Al-4V with infrared thermography, Thermosense Therm. Infrared Appl. XXXIX. 10214 (2017) 102141J. https://doi.org/10.1117/12.2263843.

[42] P. Hou, J. Fan, Q. Guo, X. Guo, The application of the infrared thermography on titanium alloy for studying fatigue behavior, Frat. Ed Integrita Strutt. 8 (2014) 21–27. https://doi.org/10.3221/IGF-ESIS.27.03.

[43] I. V. Papadopoulos, P. Davoli, C. Gorla, M. Filippini, A. Bernasconi, A comparative study of multiaxial high-cycle fatigue criteria for metals, Int. J. Fatigue. 19 (1997) 219–235. https://doi.org/10.1016/S0142-1123(96)00064-3.

[44] J. Schijve, Fatigue of structures and materials, 2009. https://doi.org/10.1007/978-1-4020-6808-9.

[45] Crossland.B, Effect of large hydrostatic pressures on the torsional fatigue strength of an alloy steel, in: Proc. Int. Conf. Fatigue Met. London, 1956: pp. 138–149.

[46] R.E. Peterson, Stress concentration factors, New York, Wiley-Interscience, 1974. 329 P. (1974).

[47] G. Nicoletto, R. Konečná, M. Frkáň, E. Riva, Surface roughness and directional fatigue behavior of as-built EBM and DMLS Ti6Al4V, Int. J. Fatigue. 116 (2018) 140–148. https://doi.org/10.1016/j.ijfatigue.2018.06.011.

[48] J. Yang, H. Yu, Z. Wang, X. Zeng, Effect of crystallographic orientation on mechanical anisotropy of selective laser melted Ti-6Al-4V alloy, Mater. Charact. 127 (2017) 137–145. https://doi.org/10.1016/j.matchar.2017.01.014.

[49] C. Flament, M. Salvia, B. Berthel, G. Crosland, Local strain and damage measurements on a composite with digital image correlation and acoustic emission, J. Compos. Mater. 50 (2016) 1989–1996. https://doi.org/10.1177/0021998315597993.

[50] L. Wagner, Mechanical surface treatments on titanium, aluminum and magnesium alloys, Mater. Sci. Eng. A. 263 (1999) 210–216. https://doi.org/10.1016/s0921-5093(98)01168-x.

[51] B.P. Haigh, Experiments on the fatigue of brasses, J. Inst. Met. 18 (1917) 55–86. https://www.scopus.com/inward/record.uri?eid=2-s2.0-0012839155&partnerID=40&md5=c6d263598fe03578509459f78228158d.

[52] J.O. Almen, P.H. Black, Residual Stresses and Fatigue in Metals, McGraw-Hill, 1963. https://books.google.fr/books?id=oTc_AQAAIAAJ.

[53] B. Vrancken, L. Thijs, J.P. Kruth, J. Van Humbeeck, Heat treatment of Ti6Al4V produced by Selective Laser Melting: Microstructure and mechanical properties, J. Alloys Compd. 541 (2012) 177–185. https://doi.org/10.1016/j.jallcom.2012.07.022.

[54] G.Q. Wu, C.L. Shi, W. Sha, A.X. Sha, H.R. Jiang, Effect of microstructure on the fatigue properties of Ti-6Al-4V titanium alloys, Mater. Des. 46 (2013) 668–674. https://doi.org/10.1016/j.matdes.2012.10.059.

[55] W.J. Dixon, A.M. Mood, A method for obtaining and analyzing sensitivity data, J. Am. Stat. Assoc. 43 (1948) 109–126.

[56] V. Honorat, S. Moreau, J.M. Muracciole, B. Wattrisse, A. Chrysochoos, Calorimetric analysis of polymer behaviour using a pixel calibration of an IRFPA camera, Quant. Infrared Thermogr. J. 2 (2005) 153–171. https://doi.org/10.3166/qirt.2.153-171.

[57] D. Especel, S. Matteï, Total emissivity measurements without use of an absolute reference, Infrared Phys. Technol. 37 (1996) 777–784. https://doi.org/10.1016/S1350-4495(96)00017-5.

[58] T. Boulanger, Analyse par thermographie infrarouge des sources de chaleur induites par la fatigue des aciers, Ph.D Thesis, Univ. Montpellier 2. (2004) 1 vol. (159 p.).

[59] A.R. Moustafa, Mesure thermographique des effets dissipatifs accompagnant le fretting : d'une construction rapide des cartes d'amorçage vers une meillleure compréhension des mécanismes d'endommagement, 2016. http://www.theses.fr/2016LYSEC012/document.

[60] B. Berthel, A.R. Moustafa, E. Charkaluk, S. Fouvry, Crack nucleation threshold under fretting loading by a thermal method, Tribol. Int. 76 (2014) 35–44. https://doi.org/10.1016/j.triboint.2013.10.008.

[61] J.-C. Krapez, D. Pacou, Thermography detection of damage initiation during fatigue tests, in: Proc. SPIE - Int. Soc. Opt. Eng., 2002: pp. 435–449. https://doi.org/10.1117/12.459593.

[62] T. Boulanger, A. Chrysochoos, C. Mabru, A. Galtier, Calorimetric analysis of dissipative and thermoelastic effects associated with the fatigue behavior of steels, Int. J. Fatigue. 26 (2004) 221–229. https://doi.org/10.1016/S0142-1123(03)00171-3.

[63] R.J. Greene, E.A. Patterson, R.E. Rowlands, Thermoelastic Stress Analysis BT - Springer Handbook of Experimental Solid Mechanics, in: W.N. Sharpe (Ed.), Springer US, Boston, MA, 2008: pp. 743–768. https://doi.org/10.1007/978-0-387-30877-7_26.

[64] R. Molaei, A. Fatemi, N. Phan, Significance of hot isostatic pressing (HIP) on multiaxial deformation and fatigue behaviors of additive manufactured Ti-6Al-4V including build orientation and surface

roughness effects, Int. J. Fatigue. 117 (2018) 352–370. https://doi.org/10.1016/j.ijfatigue.2018.07.035.

[65] M. Lieblich, S. Barriuso, M. Multigner, G. González-Doncel, J.L. González-Carrasco, Thermal oxidation of medical Ti6Al4V blasted with ceramic particles: Effects on the microstructure, residual stresses and mechanical properties, J. Mech. Behav. Biomed. Mater. 54 (2016) 173–184. https://doi.org/10.1016/j.jmbbm.2015.09.032.

[66] B. Berthel, A. Chrysochoos, B. Wattrisse, A. Galtier, Infrared image processing for the calorimetric analysis of fatigue phenomena, Exp. Mech. 48 (2008) 79–90. https://doi.org/10.1007/s11340-007-9092-2.